層状希土類化合物RZn3P3 (R=Ho,Y) の高圧合成と磁気的性質

DISSERTATION

High-Pressure Synthesis and Magnetic Properties of Layered Rare-Earth Compounds RZn$_3$P$_3$ (R = Ho, Y)

Muroran Institute of Technology

Doctor of Engineering

Course of Advanced Information and Electronic Engineering

Admission in 2018

Student ID number 18096008

Saravanan Janagan

Submission in 2020

Abstract

This thesis describes magnetic properties of layered rare earth zinc phosphide compounds RZn$_3$P$_3$(R = Ho, Y) prepared under high pressure synthesis. RZn$_3$P$_3$ (R = rare earth) crystallizes into hexagonal ScAl$_3$C$_3$ structure with $P6_3/mmc$ (space group 194). In RZn$_3$P$_3$ (R = Rare earth) compounds, rare earth atoms form 2-dimensional triangular lattice structure in the c-plane. These rare-earth-atom layers are well separated by zinc and phosphide atoms. We have studied magnetisation, electrical resistivity and specific heat measurements of the compounds. The magnetic susceptibility shows an anomaly at 5 K ascribed to a magnetic ordering. The resistivity reveals metallic nature, a low temperature minimum around 17 K, and an upturn follows logarithmic dependence of the temperature (-log T). In addition, resistivity displays a sharp drop at 4.5 K which corresponds to the magnetic ordering. The resistivity upturn was suppressed by magnetic field. The specific heat exhibits a clear kink at 4.5 K (T_M), according to magnetic ordering. The T_M shifts towards high temperature with the rate of 0.06 K/kOe. A large γ value was observed as 199 mJ/molK^2 and it increases with increasing magnetic field up to 60 kOe and decreases further. We demonstrate the crucial role of hybridization between 4f electrons and conduction electrons depending on the distance between rare earth atoms in determining transport and magnetic properties of RZn$_3$P$_3$ (R = rare earth).

Acknowledgements

Contents

List of Figures

List of tables

CHAPTER – 1

INTRODUCTION

1.1 Magnetism

1.1.1 Magnetisation and Susceptibility

Magnetisation (*M*) is magnetic moment per unit volume and for a linear compound in an applied magnetic field is given below,

M = χH

Where, *χ* is the magnetic susceptibility.

Curie- Weiss law

The Curie-Weiss law provides the susceptibility (*χ*) of a ferromagnetic material in the paramagnetic regime above the Curie point.

$$\chi = \frac{C}{T - \theta_W}$$

Where, *C* is a Curie constant

T is the absolute temperature

θ_W is the Curie temperature.

If θ_W is positive value, magnetic interaction in the compound is ferromagnetic.

If θ_W is positive value, magnetic interaction in the compound is antiferromagnetic which is denoted as Neel temperature (T_N).

1.1.2 Exchange interactions

Direct exchange

Direct exchange interaction arises due to the orbital overlap of two atoms resulting in a correlation in their atoms. Coulomb interaction is minimized, and Pauli exclusion principle obeyed as electrons align anti-parallel.

Superexchange or Kramers-Anderson superexchange

Super exchange interaction is the strong antiferromagnetic coupling between two next-to-nearest neighbour cations via a non-magnetic anion. Mostly oxygen is

the non-magnetic anion. In ferromagnetic exchange, it depends on several factors such as geometry of the orbital and angle.

Dipolar interaction

Dipolar interaction is the direct interaction between two magnetic dipoles. It is a weak and only becomes play important role in the low temperature for large moments. It is anisotropic and drops as r^{-3}.

1.2 Magnetic frustration

Magnetically frustrated compounds have getting attention due to their unconventional ordering parameters. In conventional magnets, magnetic moments construct long range order below magnetic transition temperature. Unlike conventional magnets, frustrated magnets do not order even down to 0 K and competing magnetic moments often lead to magnetically liquid states. This state is called quantum spin liquid (QSL) where spins behave like they are in liquid. Spin liquid state arise from different magnetic exchange interaction such as Heisenberg and Kitaev model (theoretically well known). Also, some potential lattice geometry give rise to spin liquids such as triangular lattice, Kagome (corner sharing triangular lattice), honeycomb, or hyperkagome. An archetypal example of magnetic frustration is when antiferromagnetically coupled atoms are arranged on a triangular lattice where one atom cannot satisfy other two atoms at the same time [1][2]. It prevents the system to form long range order and leads to magnetic frustration. Among few structures Kagome type is well studied and exhibits high degree of magnetic frustration and shown in the fig. 1. 1. Various Kagome structure compounds have been reported such as $ZnCu_3(OH)_6Cl_2$ (Herbertsmithite mineral) [3], $Na_4Ir_3O_8$ (hyper Kagome) [4][5] and $Ca_{10}Cr_7O_{28}$ (Kagome bilayer lattice) [6]. Triangular lattice shows frustration only when interaction among the atoms is antiferromagnetic. Otherwise, ferromagnetic atoms (Heisenberg interaction) on triangular lattice form ferromagnetic state without competing. Hence, there is no evidence of frustration.

Since, frustrated magnets have no long-range order in the ground state which leads to absence of symmetry breaking. Symmetry breaking or magnetic transition of the compounds can be clearly seen in magnetization or specific heat measurements. Among the reported frustrated magnets, most of them are insulators. Search for the metallic frustrated compounds is ongoing because which might offer understanding of spin liquid state coexisting with conduction electrons and reveal other electronic states.
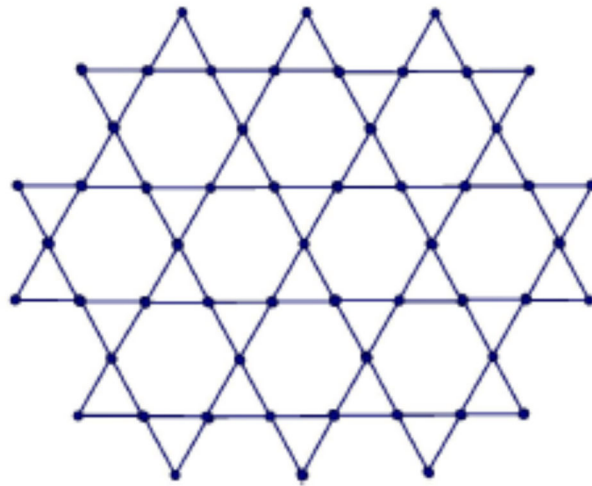
Figure 1.1 Kagome lattice structure (Corner sharing triangular lattice).
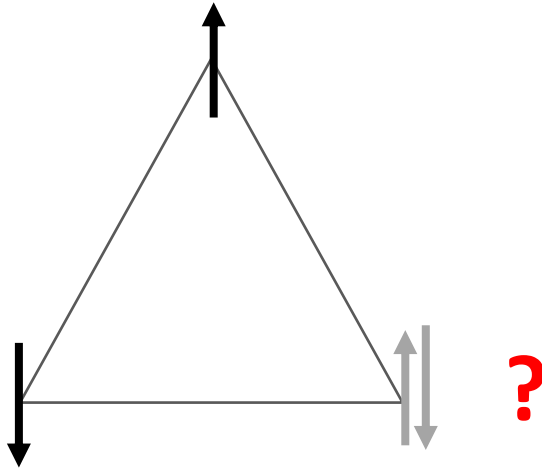
Figure 1.2 Triangular lattice with antiferromagnetically coupled spins.

1.3 Triangular Lattice (TL)

In beginning, triangular lattice structure was first proposed as potential candidate for magnetically frustrated system. Consider the antiferromagnetically interacting spins (spin - 1/2) on the corner of a triangular lattice as shown in fig. 1.2 One spin cannot arrange itself anti parallel to other two spins. Hence all three spins tend to interact minimum to minimize the energy. This interaction of every spin pair cause frustration. Compounds such as $YbMgGaO_4$ [7] and $NaYbO_2$ [8][9] have been reported as magnetically frustrated magnets due to their ideal structure. In these compounds, frustration occurs from anisotropic interaction of Yb atoms. Both compounds show no magnetic transition down to 50 mK in magnetization and specific heat measurements.

1.4 RZn$_3$P$_3$ (R = rare earth compounds)
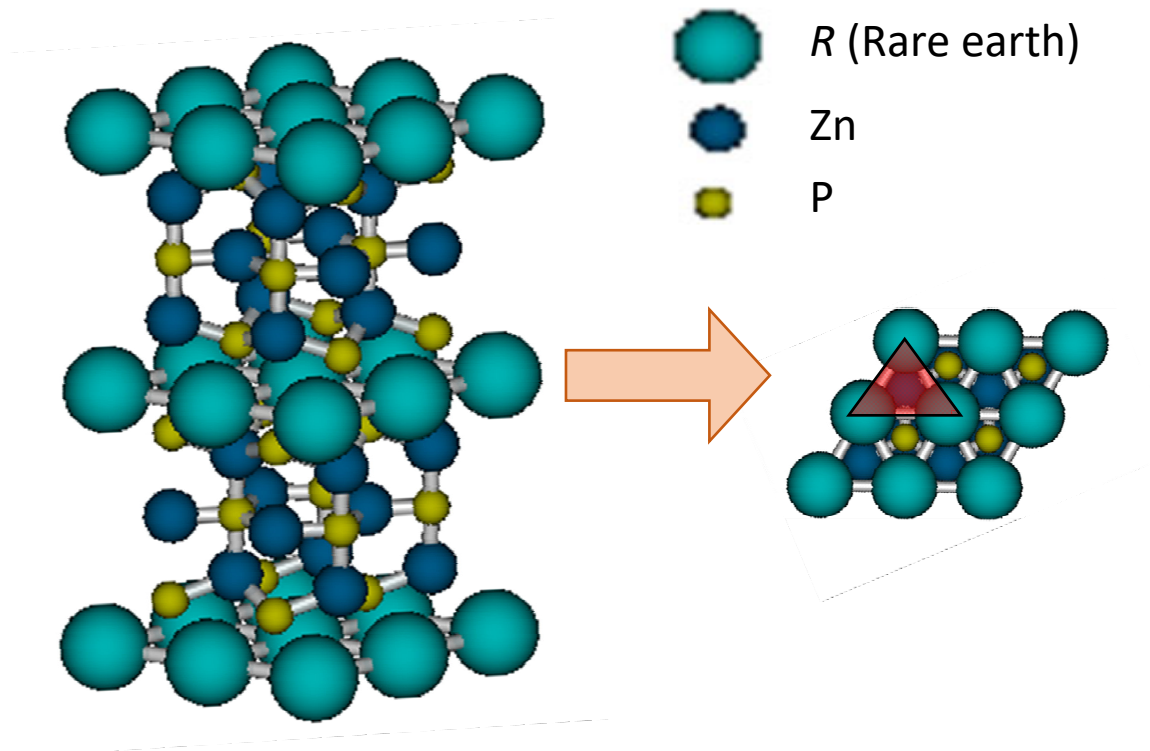
Figure 1.3 Crystal structure of RZn$_3$P$_3$ compounds. Right figure shows top view of layered rare earth compounds.

Rare earth layered Zinc Phosphide has hexagonal ScAl$_3$P$_3$ type structure with $P6_3/mmc$ [10]. Rare earth atoms form a layer between zinc and phosphide atoms. Rare earth layer consists of triangular lattice structure. The layers are well distanced by zinc and phosphide atoms. RZn$_3$P$_3$ structure is shown in fig. 1. 3.

1.5 RM_3X_3 (R = rare earth, M = Al, Cd, Zn, X = C, P, As) - 1-3-3 compounds

$YbAl_3C_3$ is a low carrier metal which exhibits spin gap state below structural transition temperature [11-13]. $CeCd_3X_3$ (X = P, As) compounds show magnetic field lifted magnetic frustration [14][15]. $CeZn_3P_3$ is a semiconductor and shows low temperature antiferromagnetic ordering at 0.8 K [16]. $CeZn_3P_3$ compound shows various properties such as reduction of energy gap under high pressure [16] and photoinduced high temperature Kondo effect [17].

Electrical resistivity of RZn_3P_3 (R = La, Ce, Pr, Nd, Sm, and Gd) have been reported recently which is shown in fig. 1.4. From the graph we can see that La, Ce, Pr atoms exhibit semiconductor nature while Nd, Sm, Gd atoms show metallic nature. In RZn_3P_3 compound, Ce, Nd, and Gd atoms show long range ordering temperature (T_N) at 0.78 K, 0.63, and 4.7 K, respectively. Only Sm atoms show two transitions at 0.34 K and 0.82 K. $PrZn_3P_3$ compound does not show any transition down to 0.1 K due to singlet ground state. All the transitions can be seen in the fig. 1.5. Magnetic properties of RZn_3P_3 compound have been reported as Ce toms much influenced by super exchange interaction and Nd, Sm, Gd (metallic) atoms are influenced by Ruderman-Kittel-Kasuya-Yosida (RKKY) interaction [18]. Long range ordering temperature and resistivity behaviour of RZn_3P_3 (R = La, Ce, Pr, Nd, Sm, and Gd) are shown in the table 1.1. Lattice parameters and Volume and c/a ratio are shown in fig. 1.6. The lattice parameters a, c, and V show decrease trend with increasing $4f-$electron which is due to lanthanide contraction. The ratio c/a shows minimum around Pr atom and increases further. This change is expected to explain electrical resistivity of RZn_3P_3.
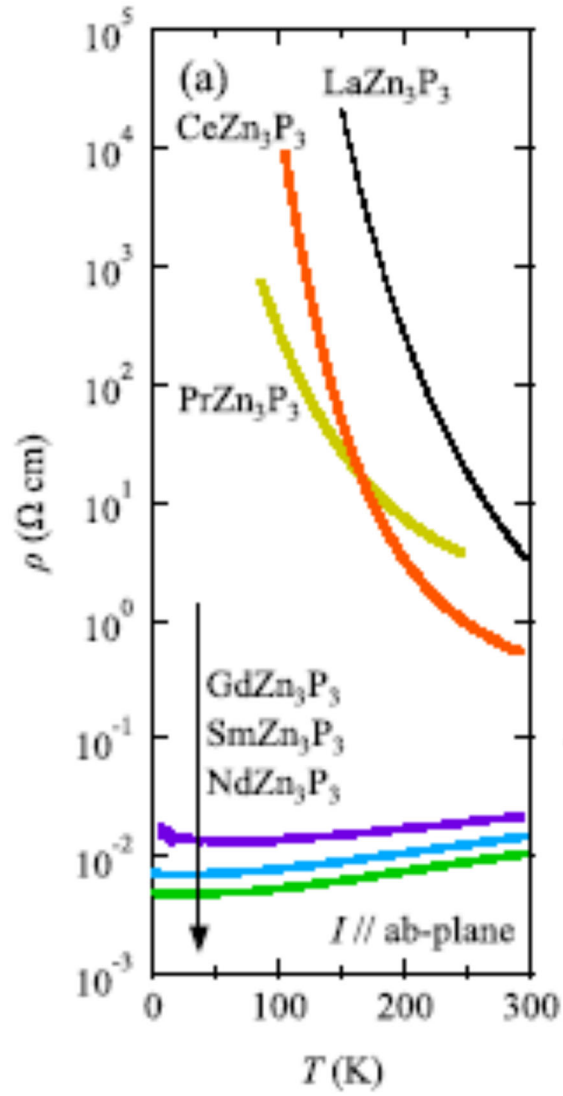
Figure 1.4 Electrical resistivity of RZn$_3$P$_3$ (R = La, Ce, Pr, Nd, Sm, and Gd)
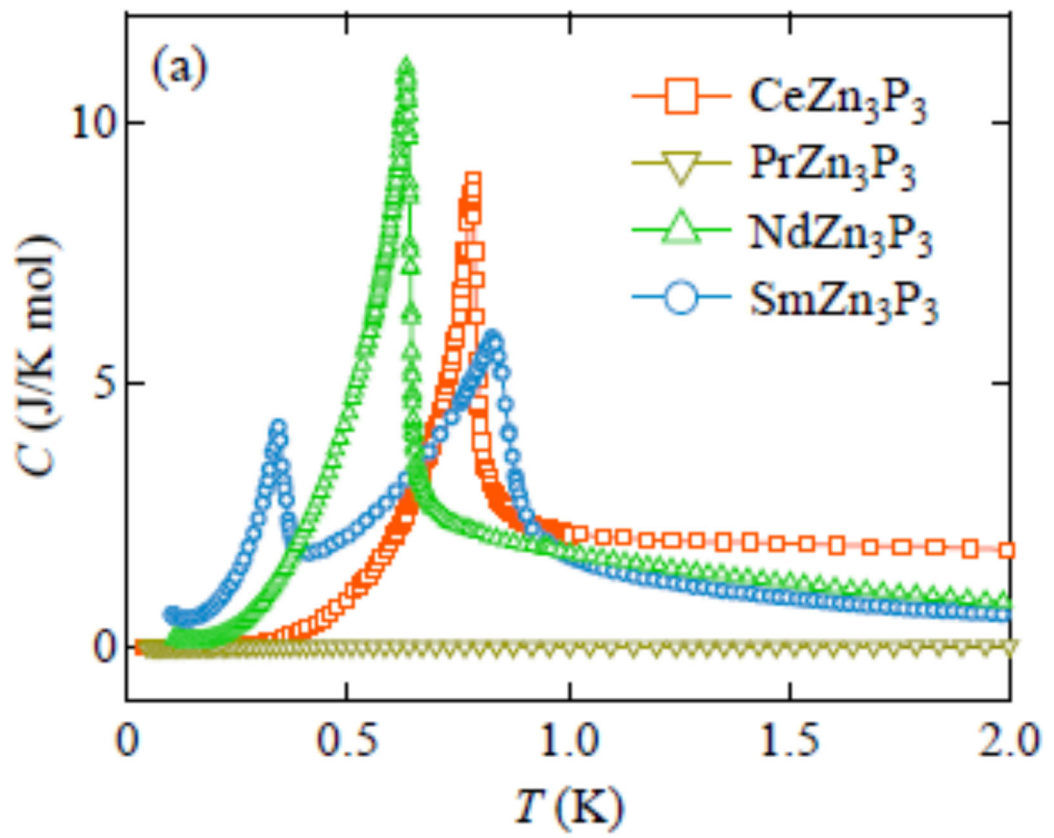
Figure 1.5 Specific heat of RZn$_3$P$_3$ (R = Ce, Pr, Nd, and Sm).

RZn$_3$P$_3$	T_N(K)	Electrical Properties
La	-	Semiconductor
Ce	0.8	Semiconductor
Pr	- (singlet)	Semiconductor
Gd	4.7	Metal
Sm	0.34 & 0.82	Metal
Nd	0.63	Metal

Table 1.1 Transition temperature and nature of RZn$_3$P$_3$ (R = La, Ce, Pr, Nd, Sm, and Gd)
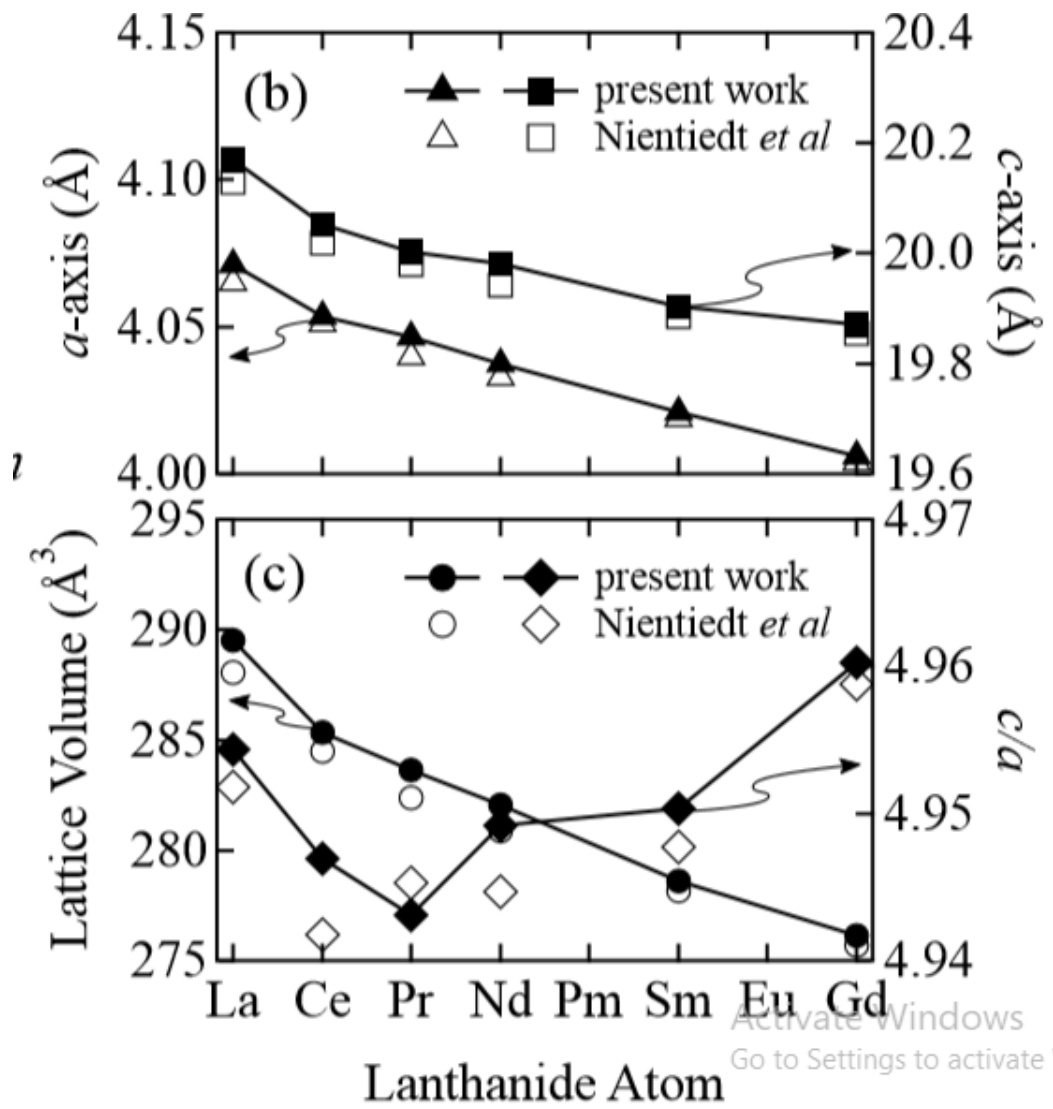
Figure 1.6 Lattice constant and volume and *c/a* ratio of *R*Zn₃P₃ (*R* = La, Ce, Pr, Nd, Sm, and Gd).

1.6 Motivation

Ho^{3+} has large magnetic moment compared to other rare earth elements and it has high number of 4f electrons. Since we are looking for various magnetic ground state Ho^{3+} might give an opportunity. And as we know number of 4f electrons and lanthanide contraction play vital role in deciding electrical nature of RZn$_3$P$_3$compounds. There is only synthesis and structural data of HoZn$_3$P$_3$ is reported [10]. There is no report of magnetic and transport properties of HoZn$_3$P$_3$. In this thesis we report magnetic and transport properties of HoZn$_3$P$_3$compounds synthesised under high pressure and high temperature technique. We expect HoZn$_3$P$_3$ compound might give an opportunity to explore relation between Kondo effect, RKKY interaction, and geometric frustration.

CHAPTER – 2

EXPERIMENTAL METHOD

2.1 In-situ X-ray observation

In-situ X-ray observation is important to find optimum conditions for synthesis such as temperature and pressure. Since we are using high pressure and high temperature technique to synthesis it is important to find optimum condition. We performed in-situ observation under high pressure and high temperature with synchrotron radiation, which is used at the beamline NE5C, Photon Factory (PF) in High Energy Accelerator Research Organization (KEK), Tsukuba, Japan. Starting materials were taken in stochiometric ratio and put in boron nitride (BN) crucible. Crucible with graphite heater is inserted into pyrophyllite cube (pressure medium). High pressure was applied by multi anvil assembly with DIA type cubic anvil apparatus and the dimensions of the assembly [19][20] which are shown in fig. 2.1. Anvil frame consists of holes in the diagonal direction to access the incident and diffracted X-ray as shown in fig. 2. 1.
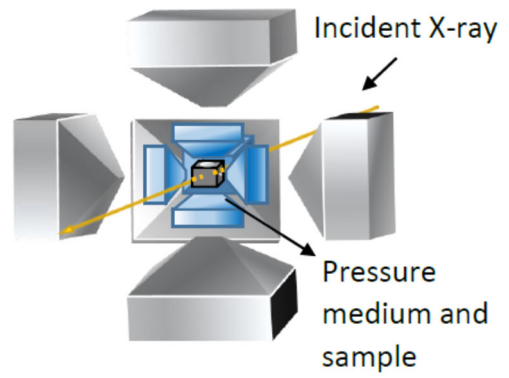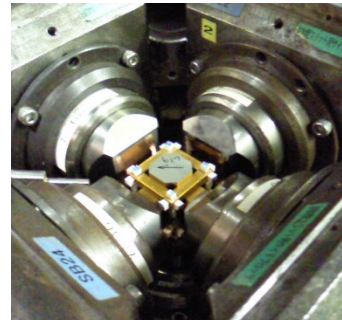
Figure 2. 1 Cubic anvil type press (MAX-80). Right top shows anvil setup and bottom shows in-situ process.

2.2 High Pressure and High Temperature Synthesis

Once we acquired optimum condition from in-situ observation, we proceed for synthesis of RZn$_3$P$_3$ compounds using high pressure and high temperature method. Starting materials were Ho, Zn chip (3N), P (5N) and taken in stochiometric ratio of 1:3:3. Then the starting materials were well mixed and filled into BN crucible. The crucible with graphite heater was placed in pressure medium (pyrophyllite cube). The sample assembly was inserted between anvils and proceeded for synthesis. The synthesis condition was pressure of 4 GPa, temperature of 875-950 °C with holding time of 90 mins. Fig. 2. 2 shows the synthesis method along with six side press using six anvils and sample assembly parts shown in fig. 2.3. For more details of HPHT synthesis and its advantages given in ref. 19, 20.

700 ton press
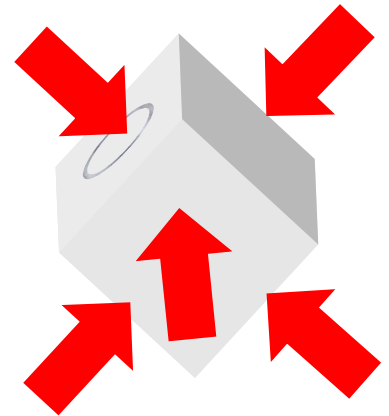
Figure 2.2 show Cubic anvil type 700 ton press. Right top shows anvil setup with sample assembly. Right bottom shows pressure applies from six side of the cube.

4.5mm

7.9mm

BN

Graphite

Pyrophyllite

Mo plate

SUS ring

Pyrophyllite cap

Figure 2.3 Sample assembly parts and dimensions.

2.3 Characterization

Synthesised samples were cut using diamond cutter, shaped, and polished using sandpaper number are 1500, 5000, and 8000, respectively. Shaped samples were subjected to X-ray diffraction method to find the structure and quality of the sample.

X- ray diffraction

In this work, we used RINT-RAPID Ⅱ with Co Kα radiation to analyse the sample as shown in fig. 2.4. CuK$_\alpha$ radiation 1.5418 Å wavelength, 40 kV, 40 mA were used conditions for this study. And a 2θ angle of 20 to 80° degree. Powder Si was used as a standard. PDXL software was used to analyse the resulting patterns. From the data we can calculate lattice parameters such as lattice constant and volume of the unit cell.

X- ray diffraction cause an Interference pattern of monochromatic X – rays in an atom of the crystal. X – rays are generated by a cathode ray tube which is monochromatic radiation directed toward the sample. Once the Bragg's law is satisfied the interference pattern will be obtained. Bragg's law is given in equation 2.1.

$$n\lambda = 2d \sin \theta \qquad\qquad 2.1$$

where,

n is a positive integer,

λ is wavelength of the incident ray,

d is distance of the crystal layers.

θ is the incident angle.

Figure 2.4 XRD (RINT-RAPID II) at Muroran Institute of Technology.

The diffractometer consists of three basic parts such as X – ray tube, sample holder and detector. Heating filament produces X – ray in a cathode ray tube and the electrons are accelerating by applying voltage to target material. Characteristic spectra are produced when electrons get enough energy to penetrate inner shell of the target material. Copper (Cu) is the common target material for single crystal diffraction which is CuK_α radiation equal to 1.5418 Å. The sample holder and detector rotate then the intensity of the reflected X – rays are collected. A detector processes the collected rays and converts into a count rate. Then the count rate can be analysed by computer. X- ray working principle is shown in fig. 2.5. Also, schematic diagram of the goniometer is shown fig. 2.6.
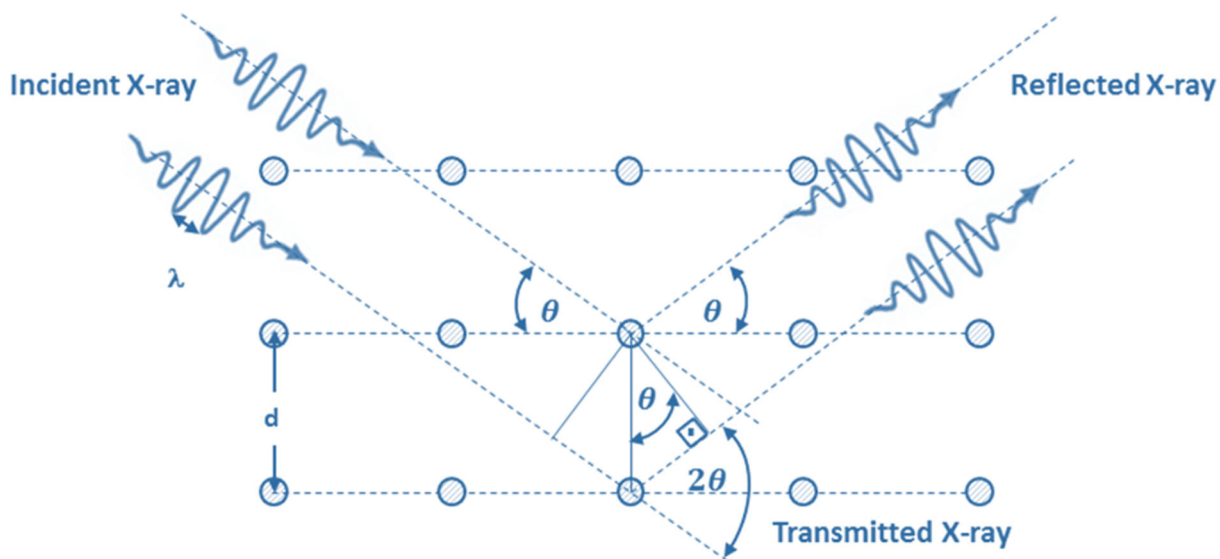
Figure 2.5 Working principle of X – ray analysis.
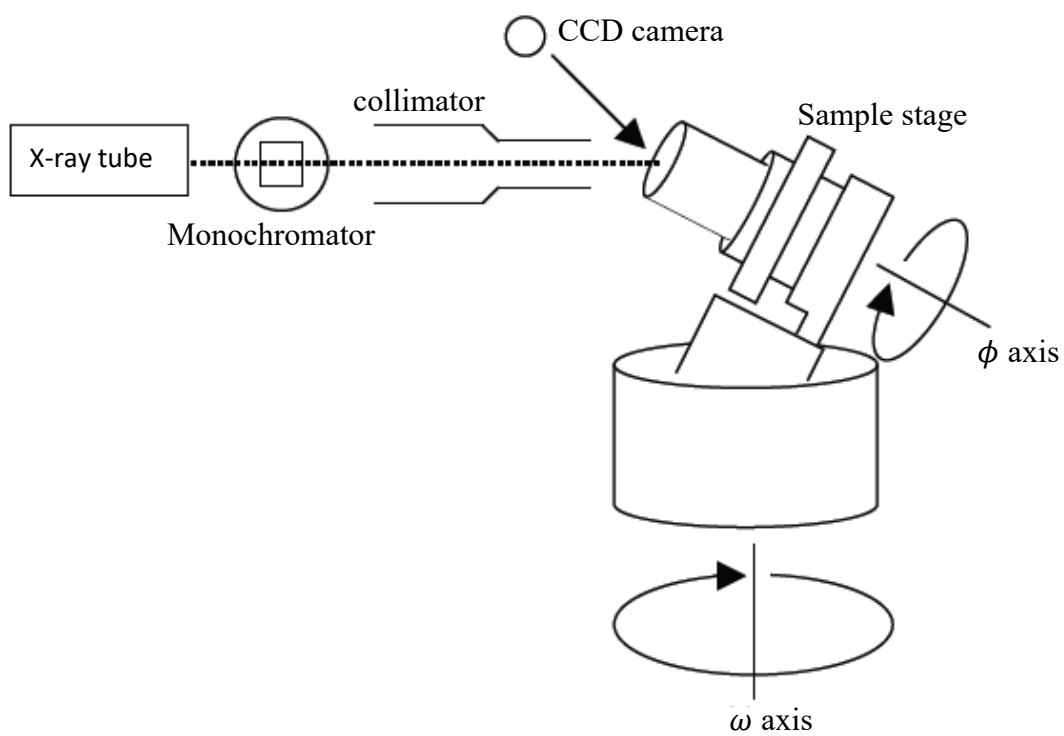
Figure 2.6 Schematic diagram of the goniometer.

Lattice parameters

The lattice constant is the physical dimension of unit cells in the crystal structure. Three-dimensional lattice has three lattice constant such as a, b, and c. There are seven crystal structures such as cubic, tetragonal, monoclinic, orthorhombic, rhombohedral, hexagonal, and triclinic which are subdivided into 14 types of lattice systems depend on lattice structure. Deviation of the peak from the original position applied in equation 2.2 and the angle correction curve is obtained from the least square fit.

$\Delta 2\theta = a_1 + a_2\cos\theta + a_3\sin 2\theta$ (2.2)

Where, a1 is the deviation from the origin of the 2θ,

a2 is eccentricity of the sample with respect to the central axis of the goniometer,

a3 is sample position and absorption.

a1, a2, and a3 are calculated by the least square fit. We used the expression 2.3 to calculate lattice constant which involves lattice constant (a, b, c), plane index (h k l), and plane spacing (d) of a hexagonal system. The equation is,

$$\frac{1}{d^2} = \frac{4}{3}\left(\frac{h^2 + hk + k^2}{a^2}\right) + \frac{l^2}{c^2}$$ 2.3

2.4 Magnetic Property Measurement System

2.4.1 Magnetic properties

Magnetic susceptibility and magnetic field dependence magnetization were performed in SQUID (Superconducting Quantum Interference Device) magnetometer (Quantum Design MPMS) at Muroran Institute of Technology which is shown in fig.2.7. MPMS is sensitive magnetometer because liquid helium cooled SQUID magnet which measures the change in the magnetic flux accurately as the sample between the superconducting detection coil. In MPMS, temperature until 2 K and magnetic field up to 7 T can be obtained. In this study we measured temperature dependence of magnetisation at different magnetic field and magnetic field dependence was measured up to 7 T at various temperature.

The magnetization is the vector field which states the density of magnetic dipole moment in the material. Magnetisation is given below,

$$M = \mu_{total} / V \qquad\qquad 2.4$$

The magnetic susceptibility (χ) is the degree to which a compound will be magnetised under an applied magnetic field. It is the ratio of magnetization of the material and external magnetic field. Magnetic susceptibility classifies the magnetism of the material such as paramagnetic (positive susceptibility) or diamagnetic (negative susceptibility). It is defined per mole of the sample.

$$\chi = M / H \text{ [emu/cm}^3] \qquad\qquad 2.5$$

SQUID magnetometer is shown in fig.2.8. In this system, sample moves in a coil consists of a two-dimensional differential gradiometer with three coils. So, we must prepare the sample a rectangular parallelepiped shape which was put into a straw a direction parallel. Then the straw on side was taped with the SQUID rod. This rod moves up and down during the measurement, so we must fix it properly. Carefully the rod with sample was inserted into the chamber. Apply magnetic field and set the temperature range for the desired measurement. Output signal and sample position can be confirmed as shown in the fig. 2.9. We use the straw due to negligible magnetisation.

Figure 2.7 SQUID – Magnetometer at Muroran Institute of Technology.
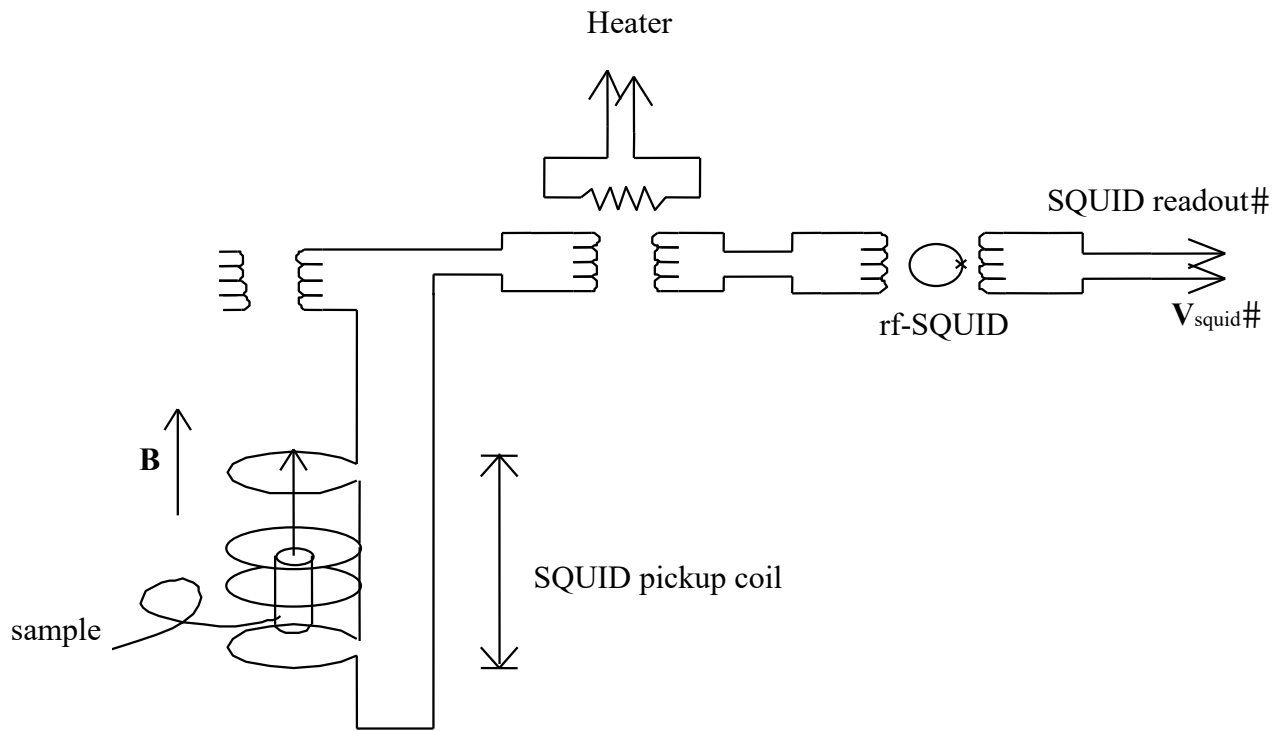
Figure 2.8 SQUID – Magnetometer schematic diagram.
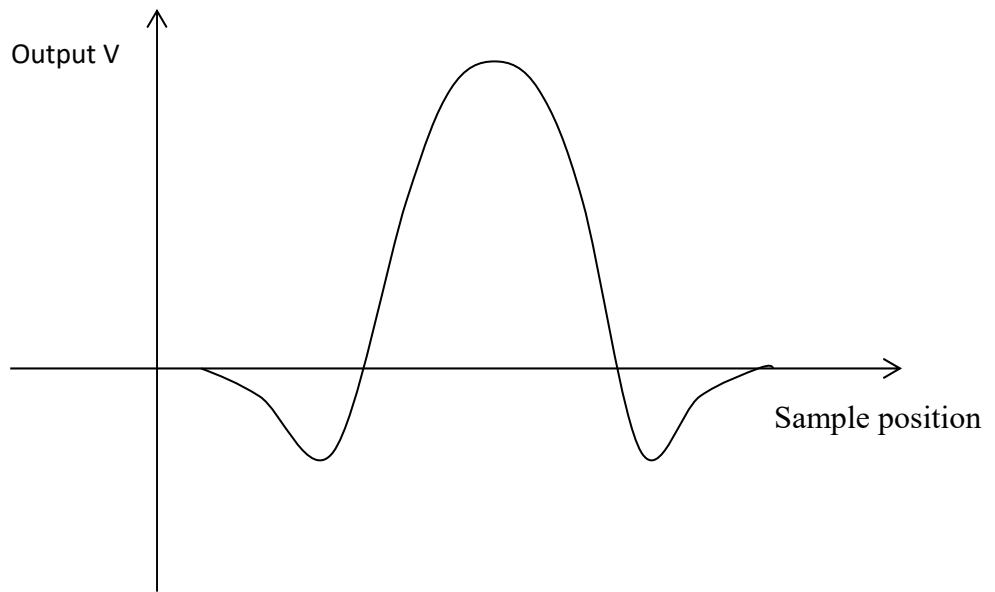
Figure 2.9 Sample position and output signal confirmation.

2.5 Physical Property Measurement System (PPMS)

2.5.1 Electrical resistivity

Good quality sample was shaped in rectangle to measure resistivity. Resistivity was measured using standard four probe method in Physical Properties Measurement System (Quantum Design PPMS). Quantum design PPMS at Muroran Institute of Technology is shown fig. 2.10. Resistivity contacts were made using copper wire and silver paste. Resistivity was measured for the temperature range of 2 K to 300 K under magnetic field of up to 7 T. Four probe method is efficient method to measure resistivity more accurately. Four probe method contact is shown in fig. 2.11.

Figure 2.10 Quantum design PPMS at Muroran Institute of Technology.
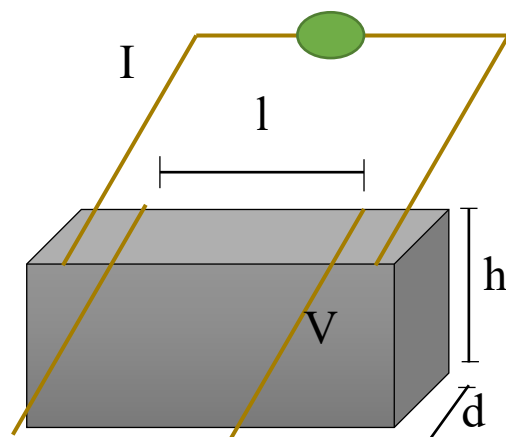
Figure 2.10 Four probe contact method with rectangular sample shape.

PPMS probe

Magnet

Thermometer

Seal sample space

Cooling annulus

Puck

Heater & Thermometer

Dual impedance system
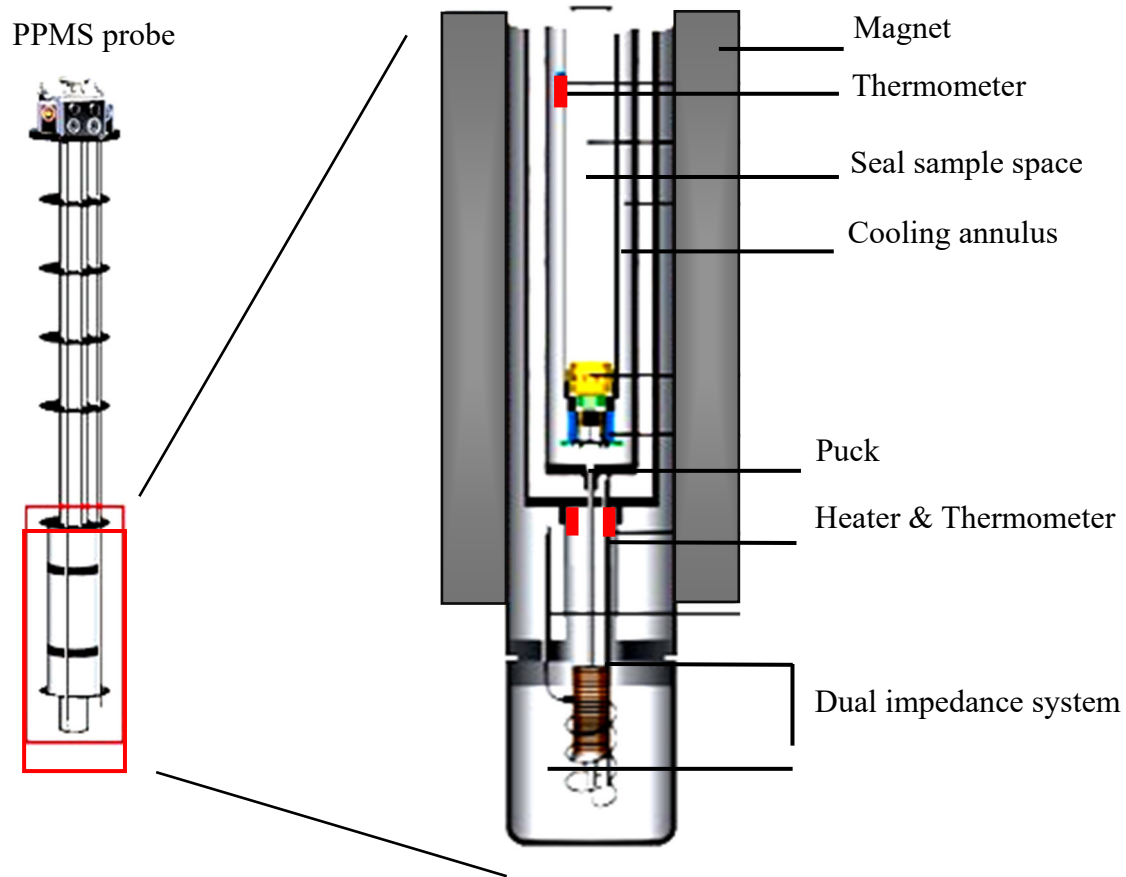
Figure 2.11 Schematic diagram of Quantum design – PPMS.

2.5.2 Specific heat capacity

Sample weight was reduced to less than 10 mg to measure specific heat measurements. Specific heat was carried out using Physical Properties Measurement System (Quantum Design PPMS) in relaxation method. The temperature range of from 2 K to 300 K and the magnetic field up to 7 T was obtained in Quantum Design PPMS.
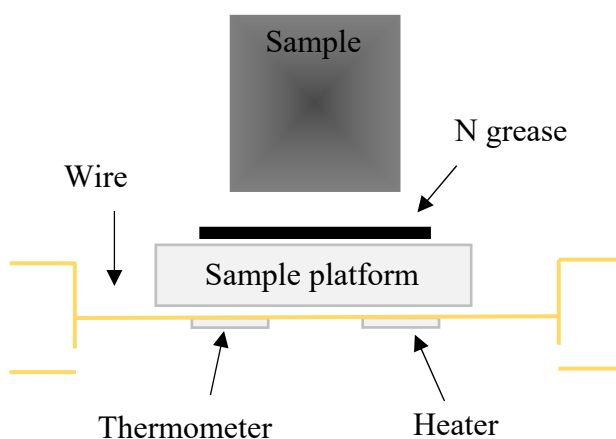
Figure 2.12 Puck for measure specific heat

Heat capacity is the amount of heat needed to increase the temperature of the material by 1 K. Specific heat capacity of a material is heat capacity of the sample divided by mass of the sample. Specific heat capacity reveals magnetic or structural transition of the compound. Also, entropy can be deduced, and ground sate properties can be predicted from specific heat capacity.

Heat capacity is the ratio of the amount of energy transferred to a compound and difference in temperature which is produced. The expression is

$$C = Q / \Delta T \qquad\qquad 2.6$$

Where, C is the heat capacity

Q is energy in joules.

Δ*T* is the difference in temperature in Kelvin.

This equation can be written another way as well. The energy is

$$Q = C \, \Delta T$$

Specific heat is divided into few methods such as relaxation method, adiabatic method, and AC method. We used the relaxation method to measure specific heat at constant pressure of the solid. The relaxation method measures the sample when the sample is not heating, and this is relaxation phenomenon. PPMSsystem controls the heat applied and removed in the sample accurately. Fig. 2.12 shows the sample puck for the specific heat measurement. The sample is placed on the sample platform with N grease. Under the sample platform, thermometer which is to measure the temperature of the puck and heater to apply the heat to sample. Thin layer of N grease increases the contact of sample to the platform and fix the sample. Sample weight of 1 mg to 200 mg can be measured in this system. But for realistic measurement sample weight of 8 – 10 mg is ideal for the measurement. High sample weight can take huge time to complete the experiment.

Once we fix the sample in the puck, we check the system for ideal condition such as 0 T and 300 K. Then we vent the chamber to ambient pressure and install the puck in the system as shown in the fig. 2.11. There is a tool for sample installation in the chamber. After insertion, we need to purge the chamber using PPMS computer. Then apply the desired magnetic field and set the temperature from 300 K to 25 K at the rate of 10 K in the sequence. Then 25 K to 10 K with increment of 1 K per minute. We must wait 1800 sec or 2400 sec at 10 K before setting 2 K which is to minimize the time. Then 10 K to 2 K measurement with the increment of 0.3 K was done. We repeat this if we want to measure at different applied field.

CHAPTER – 3

RESULT and DISCUSSION

3. 1 Powder X-Ray Diffraction

Figure 3. 1 shows X ray diffraction pattern of $HoZn_3P_3$ sample at room temperature and ambient pressure. PDXL software was used to analysis the resulting diffraction pattern. Main peaks are indexed with $P6_3/mmc$ (space group 194). From the diffraction pattern hexagonal crystal structure is confirmed. Impurities peaks were compared with major peak and less than 6 % of impurity phase confirmed. The observed impurity phases are ZnP2, Zn3P3 and P noted in the figure as open diamond, circle and square, respectively.

We deduced the lattice parameters as a = 3.9794 Å, c = 19.765 Å, and the volume of the unit cell V = 271.06 $Å^3$. The calculated lattice parameters are well matched with previous data and consistent with lanthanide contraction as ionic radius decreases [10]. X ray diffraction of YZn_3P_3 is shown in fig. 3.2. Small impurities peak such as YZnPO and Zn_3P_2 has been observed.
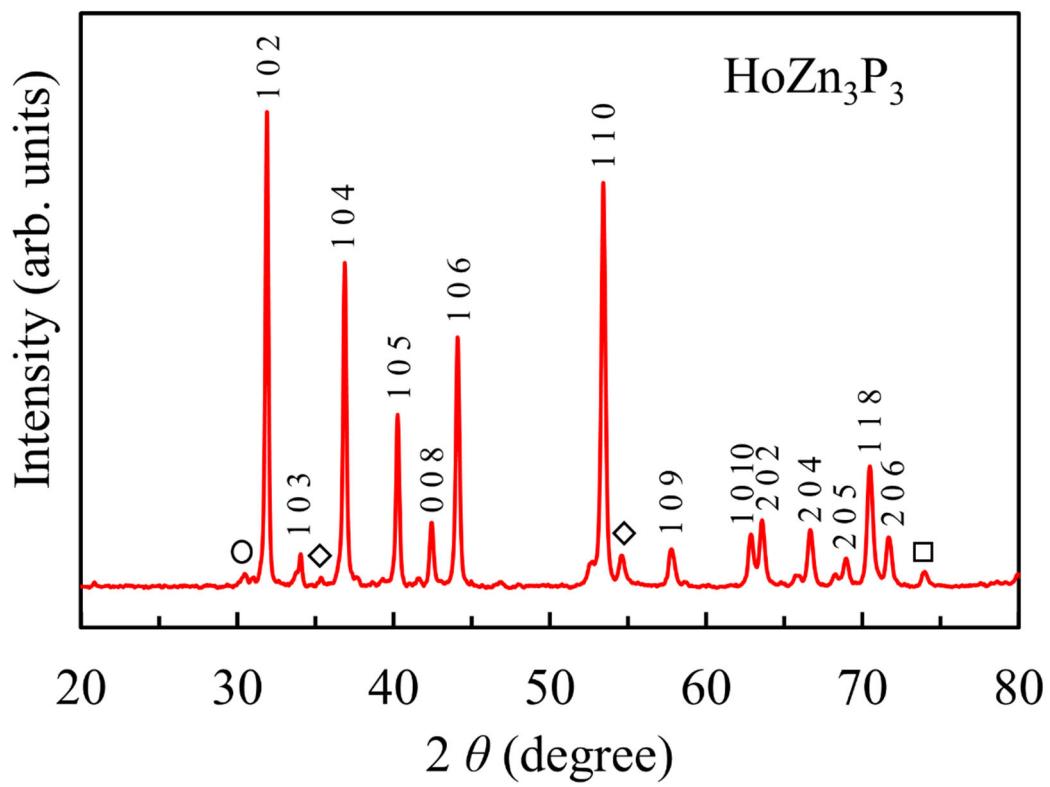
Figure 3. 1 Powder X-ray diffraction of HoZn$_3$P$_3$.
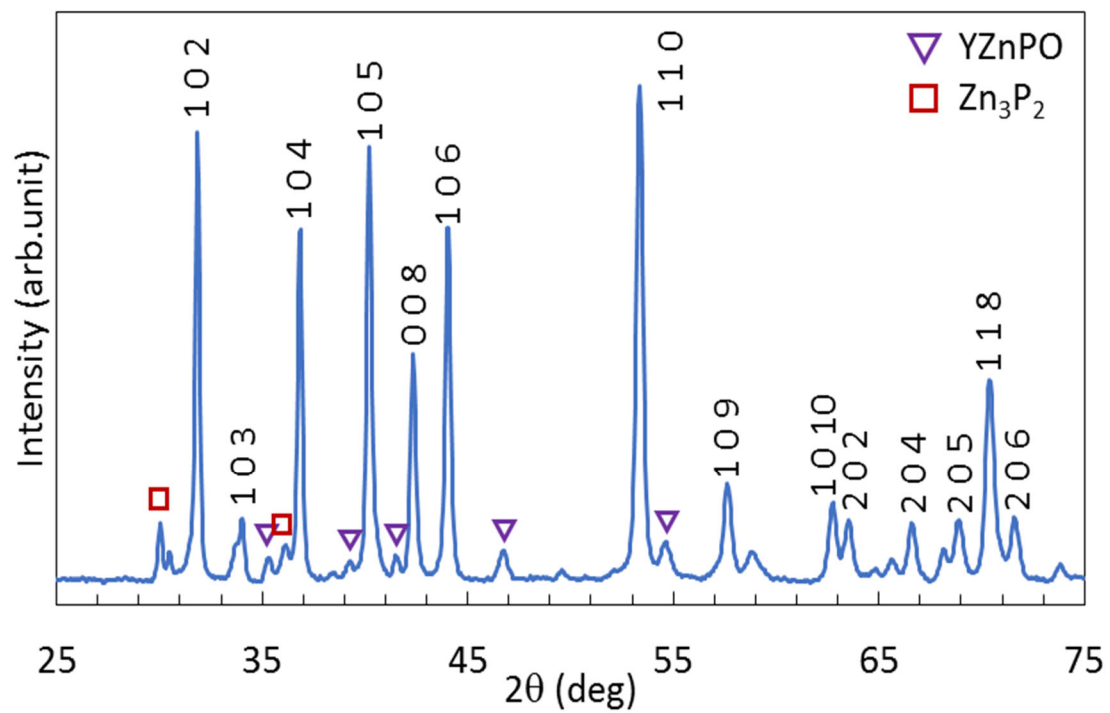
Figure 3. 2 Powder X-ray diffraction of YZn$_3$P$_3$.

3. 2 Magnetic Properties

Magnetic Susceptibility and inverse susceptibility of $HoZn_3P_3$ with magnetic field of 1 kOe is shown in fig. 3.2 and fig. 3.3. Inverse susceptibility is fitted with Curie Weiss law which can be seen along with experimental data in fig. 3.3. Red solid line is a fit from Curie Weiss law. Fig. 3.4 shows low temperature inverse susceptibility with fit and inverse susceptibility deviates at 4.5 K from the fit.

Inverse susceptibility obeys Curie Weiss law for wide temperature range which can be seen from the figure. Curie Weiss law is fitted for high temperature (150 – 300 K) and low temperature (6 – 13 K) and obtained parameters are listed in table 1. Negative Weiss temperature indicates antiferromagnetic coupling. Large difference of the parameters might be due to strong spin orbit coupling of 4 f electron or magnetic frustration induced by crystal structure.
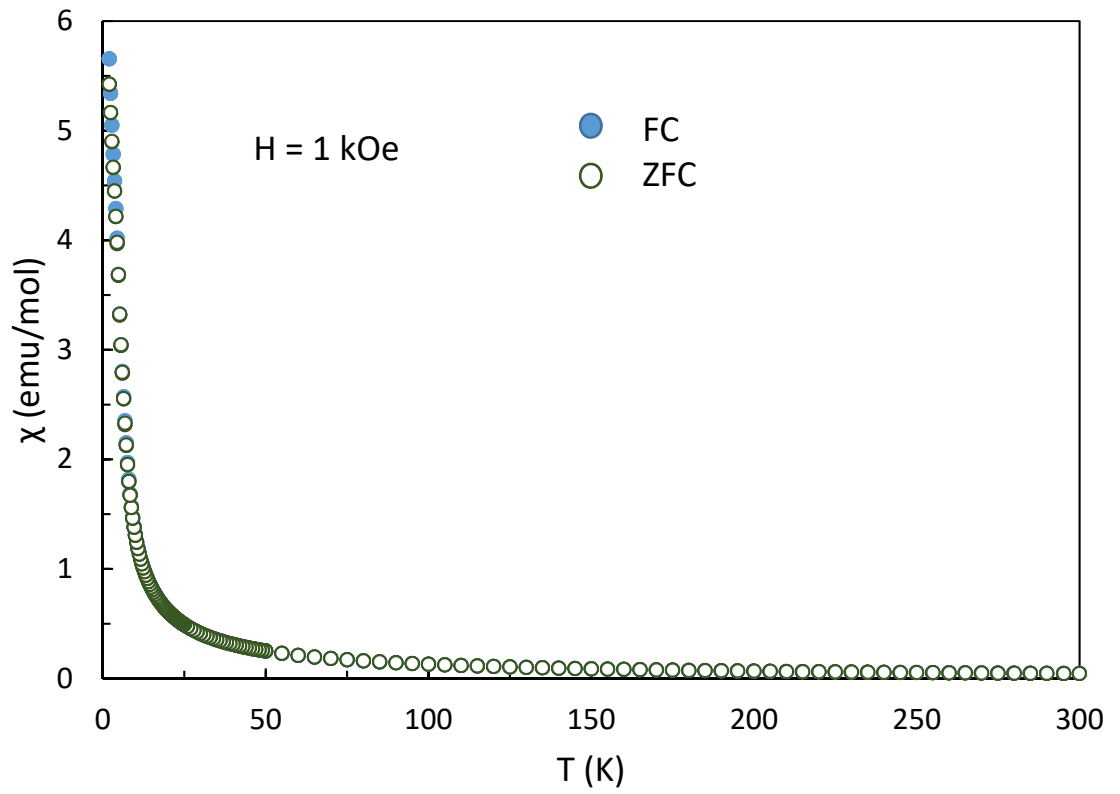
Figure 3. 3 Temperature dependence of magnetic susceptibility of HoZn$_3$P$_3$.
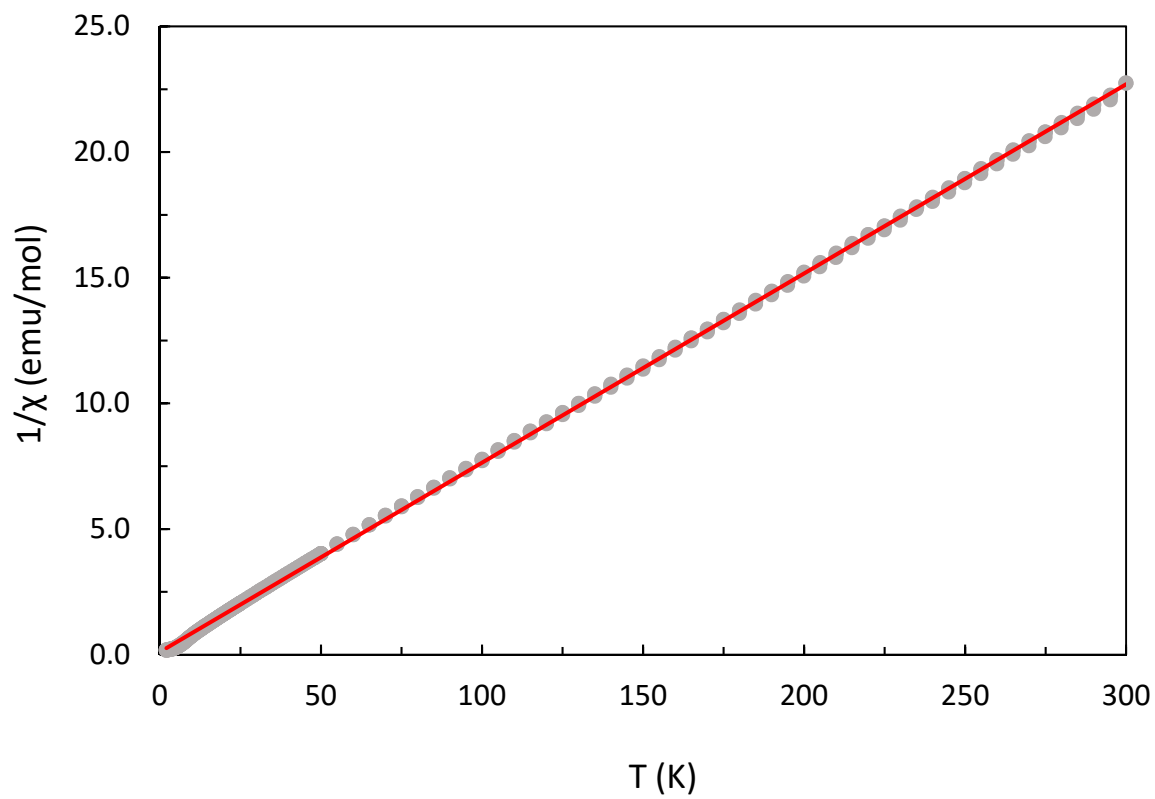
Figure 3. 4 Temperature dependence of inverse magnetic susceptibility of HoZn$_3$P$_3$.
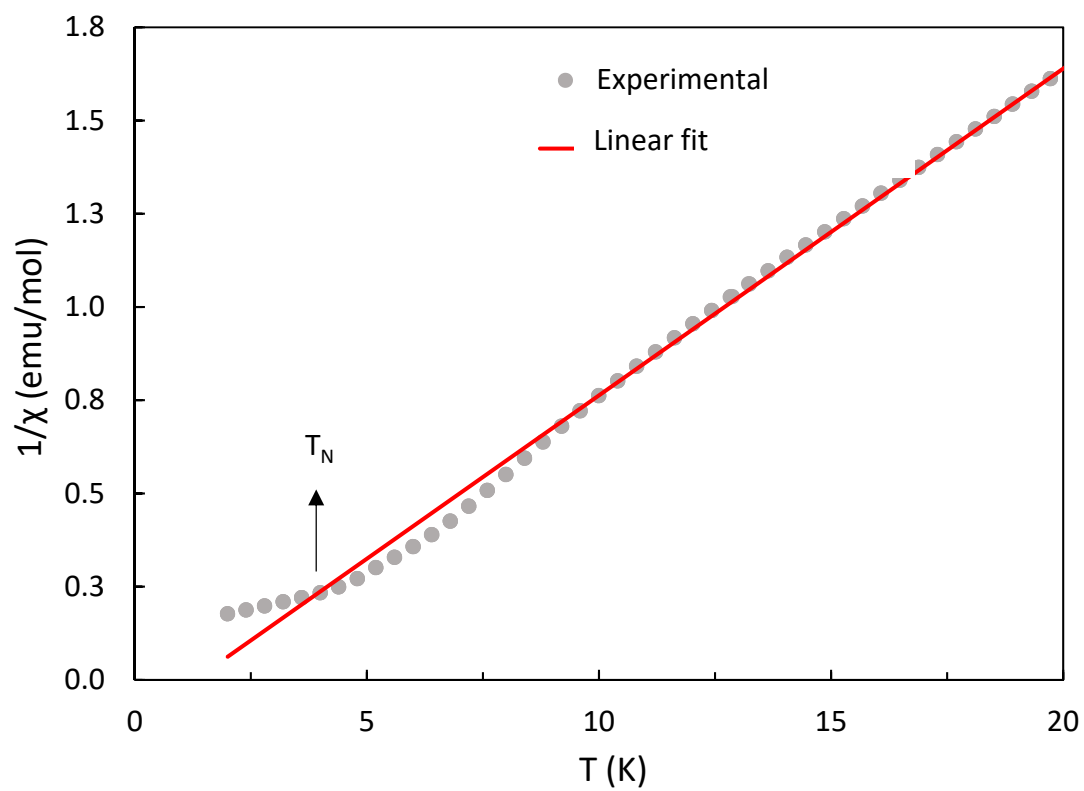
Figure 3. 5 Temperature dependence of inverse magnetic susceptibility of HoZn$_3$P$_3$ at low temperature.
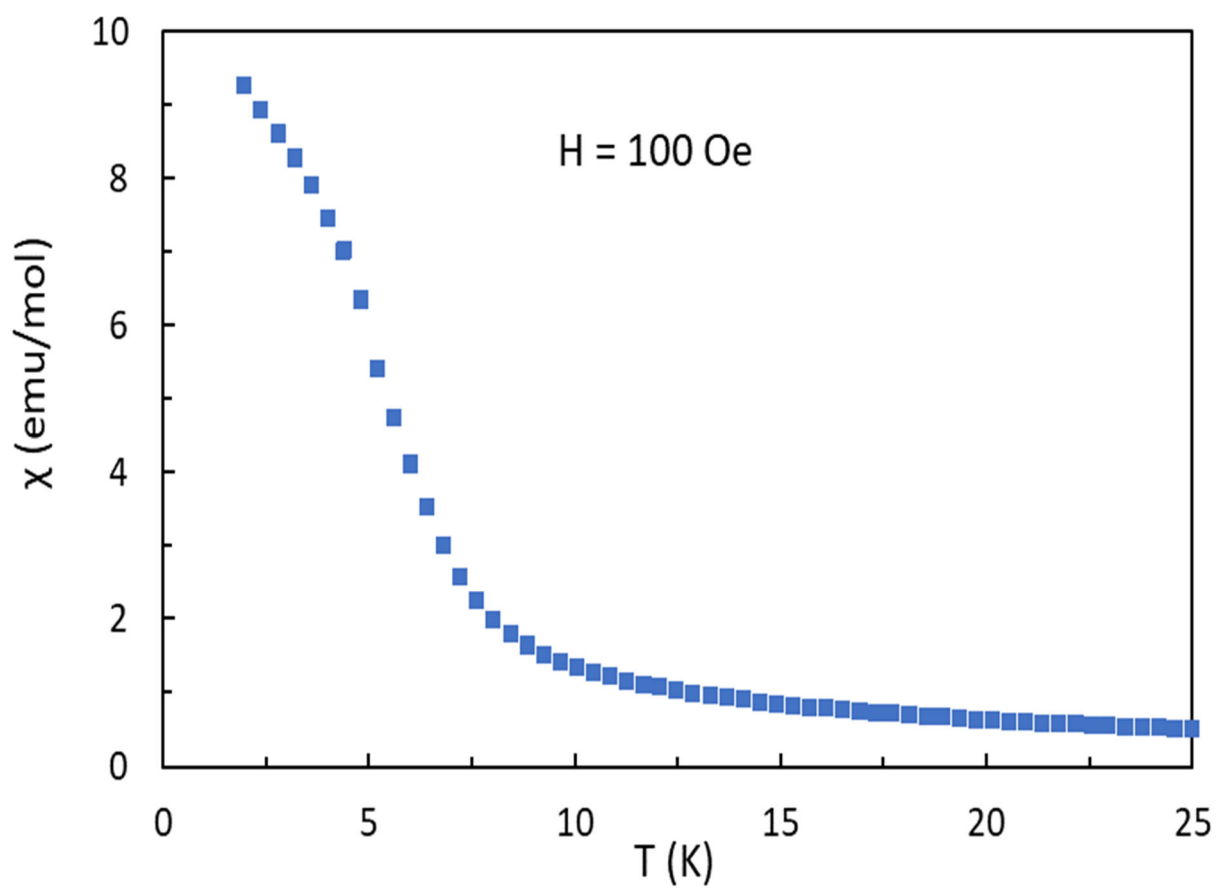
Figure 3. 6 Temperature dependence of magnetic susceptibility of HoZn$_3$P$_3$ at 100 Oe under 25 K.
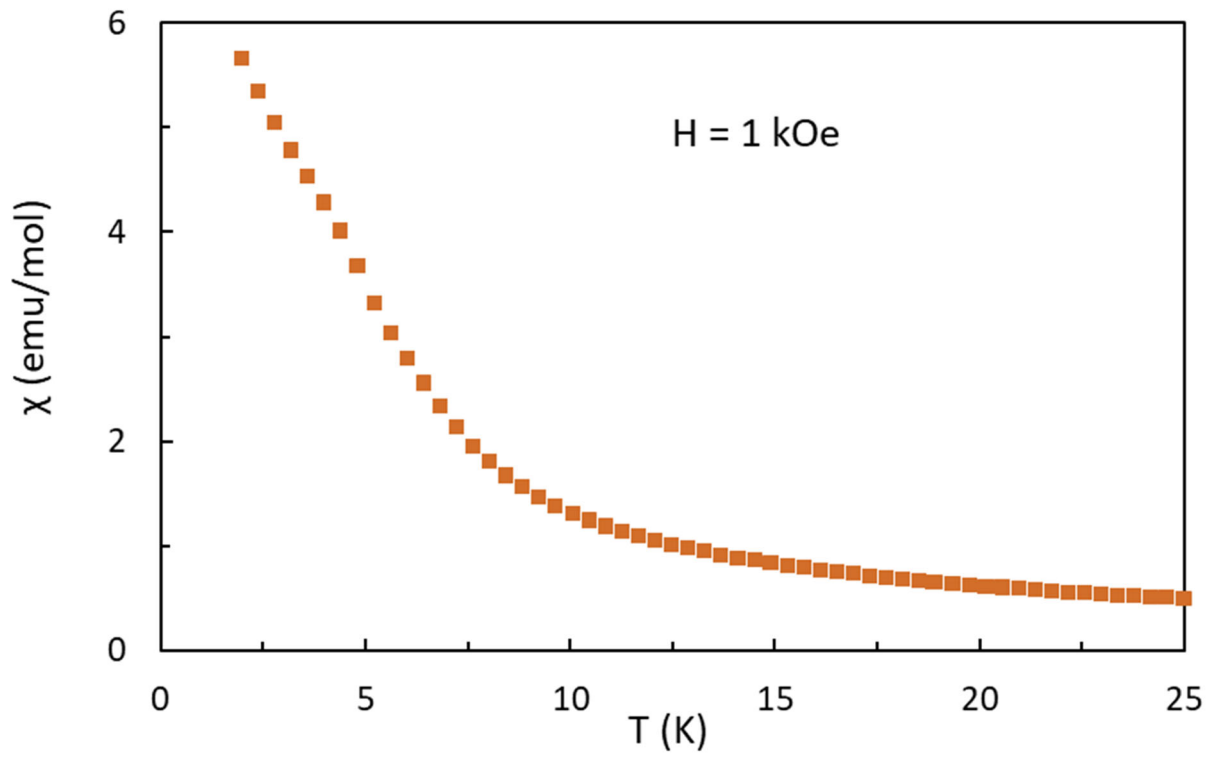
Figure 3. 7 Temperature dependence of magnetic susceptibility of HoZn$_3$P$_3$ at 1 kOe under 25 K.
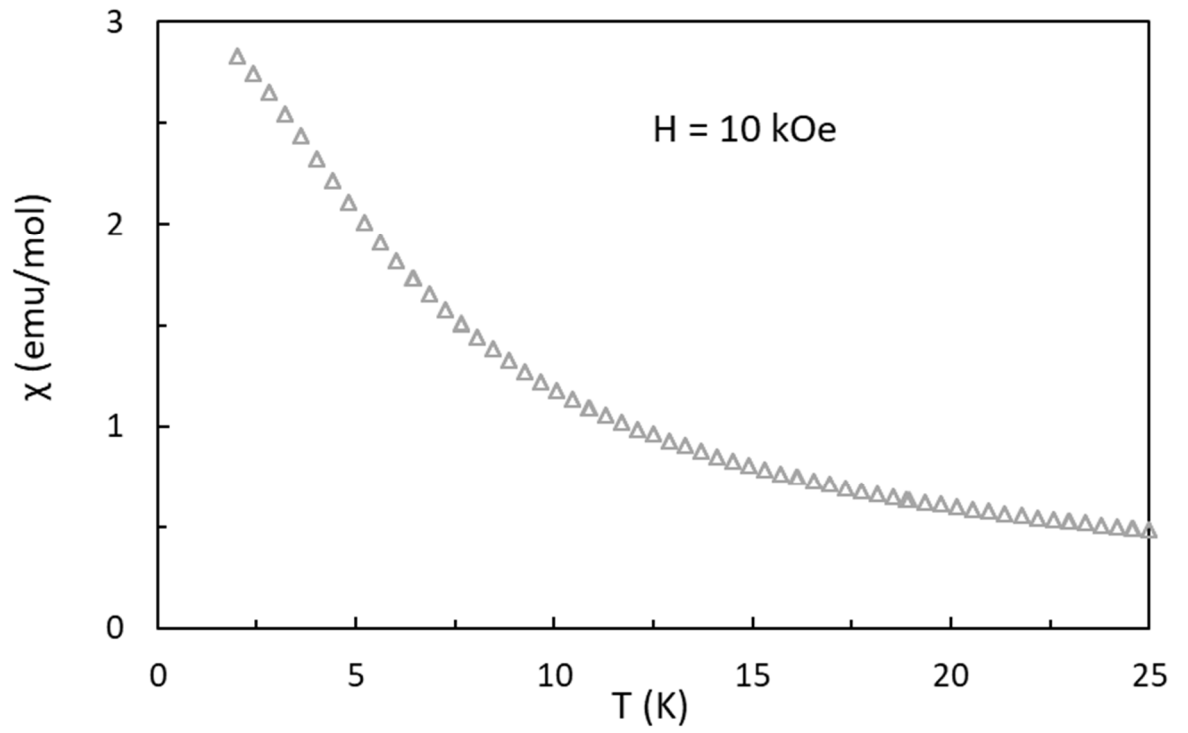
Figure 3. 8 Temperature dependence of magnetic susceptibility of $HoZn_3P_3$ at 10 kOe under 25 K.
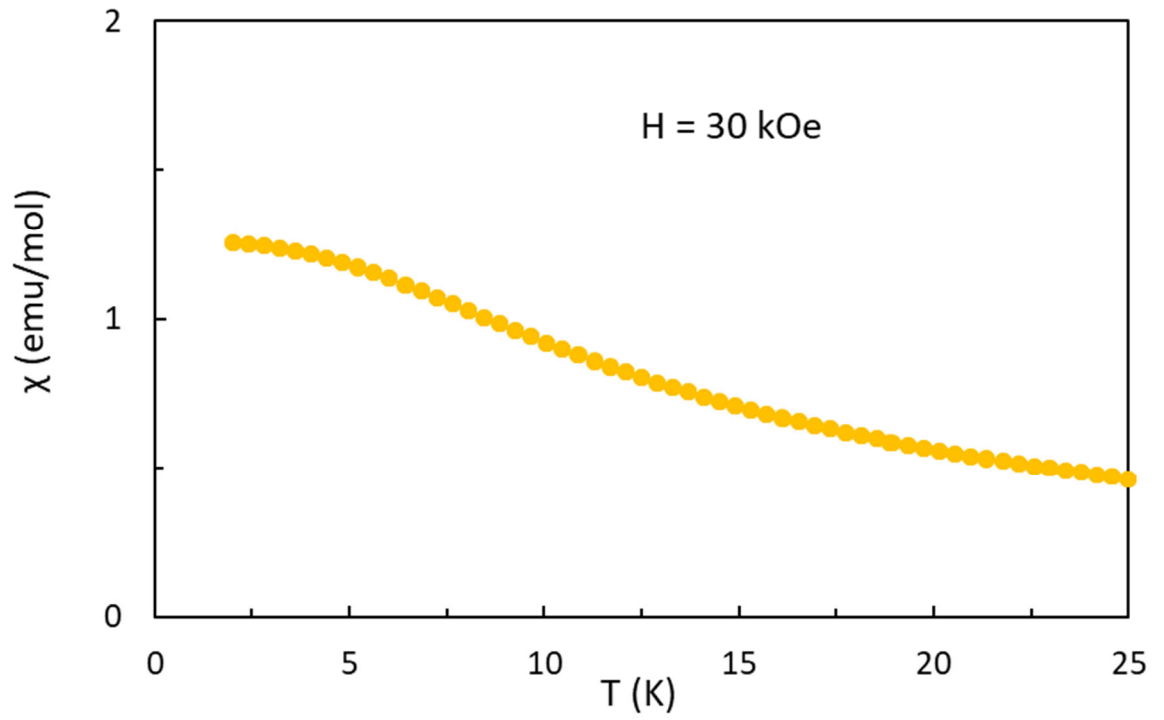
Figure 3. 9 Temperature dependence of magnetic susceptibility of HoZn$_3$P$_3$ at 30 kOe under 25 K.
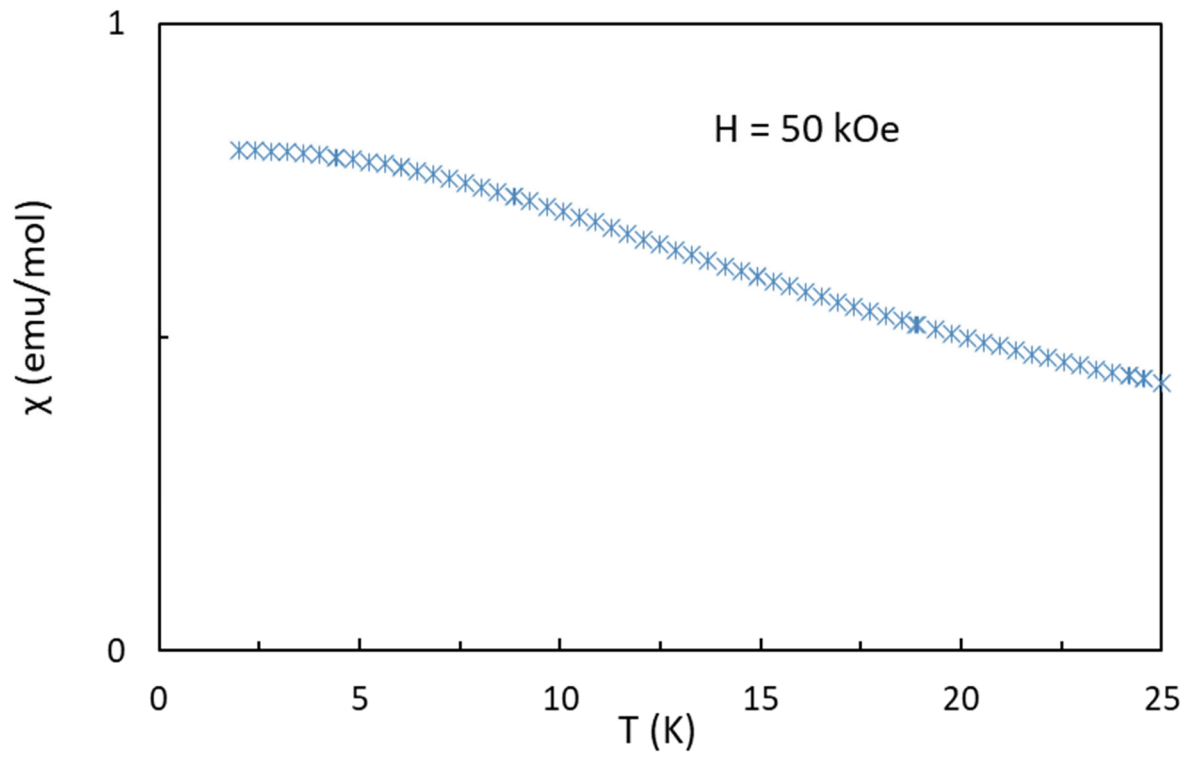
Figure 3. 10 Temperature dependence of magnetic susceptibility of $HoZn_3P_3$ at 50 kOe under 25 K.
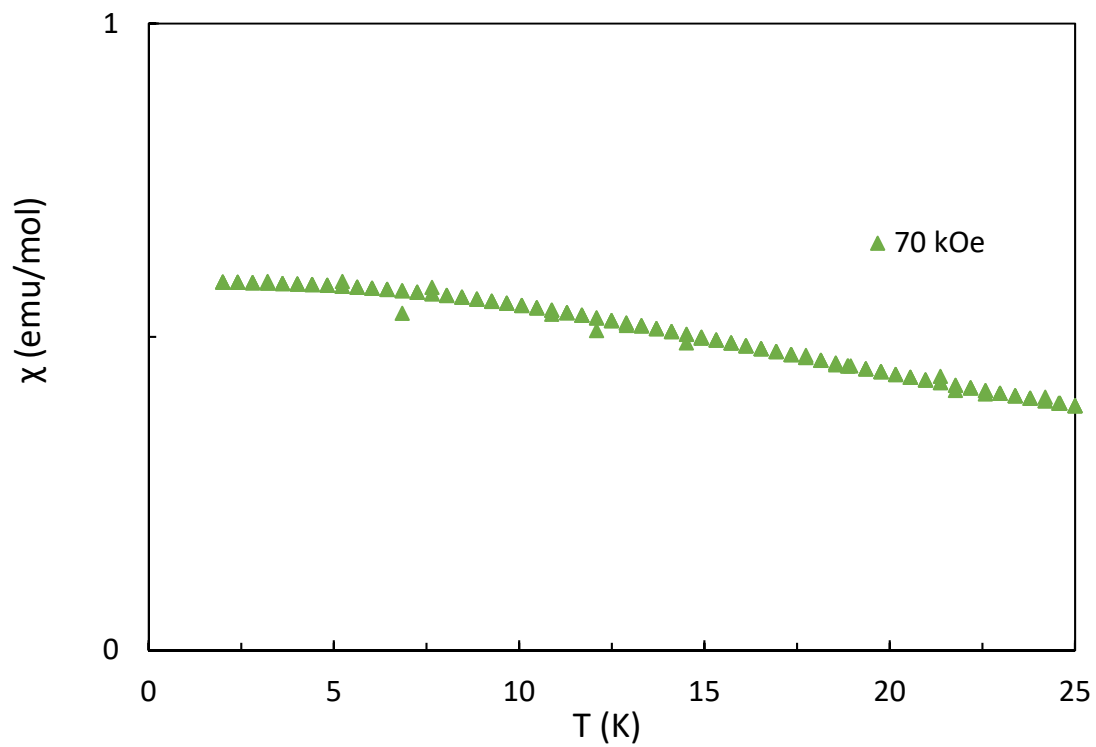
Figure 3. 11 Temperature dependence of magnetic susceptibility of HoZn$_3$P$_3$ at 70 kOe under 25 K.

	Weiss temperature (ϑ)	Effective magnetic moment (μ_{eff})
High temperature (150 – 300 K)	- 4.3 K	10.4 μ_{eff}/Ho
Low temperature (6 – 13 K)	+2.4 K	8.97 μ_{eff}/Ho

Table 3.1 Calculated Weiss temperature and effective moment.

Temperature dependence susceptibility at various field is shown in fig. 3.5-3.10. ZFC and FC curve is observed at 100 Oe at below 5 K which could be magnetic transition (T_M). This suggests possibility of strong magnetic anisotropy or canted ferromagnetic ordering. With increasing field, inflection point moves towards high temperature and disappears at high magnetic field.

Figure 3.11-15 shows magnetic field dependence magnetization of $HoZn_3P_3$ at different temperature. Magnetization curve shows Brillouin function type behaviour. At lowest accessible temperature 2 K, the magnetization reaches 4.1 μ_B/Ho which very smaller than the value of Ho magnetic moment (10 μ_B/Ho). For 2 K, magnetization was measured for increasing and decreasing field.
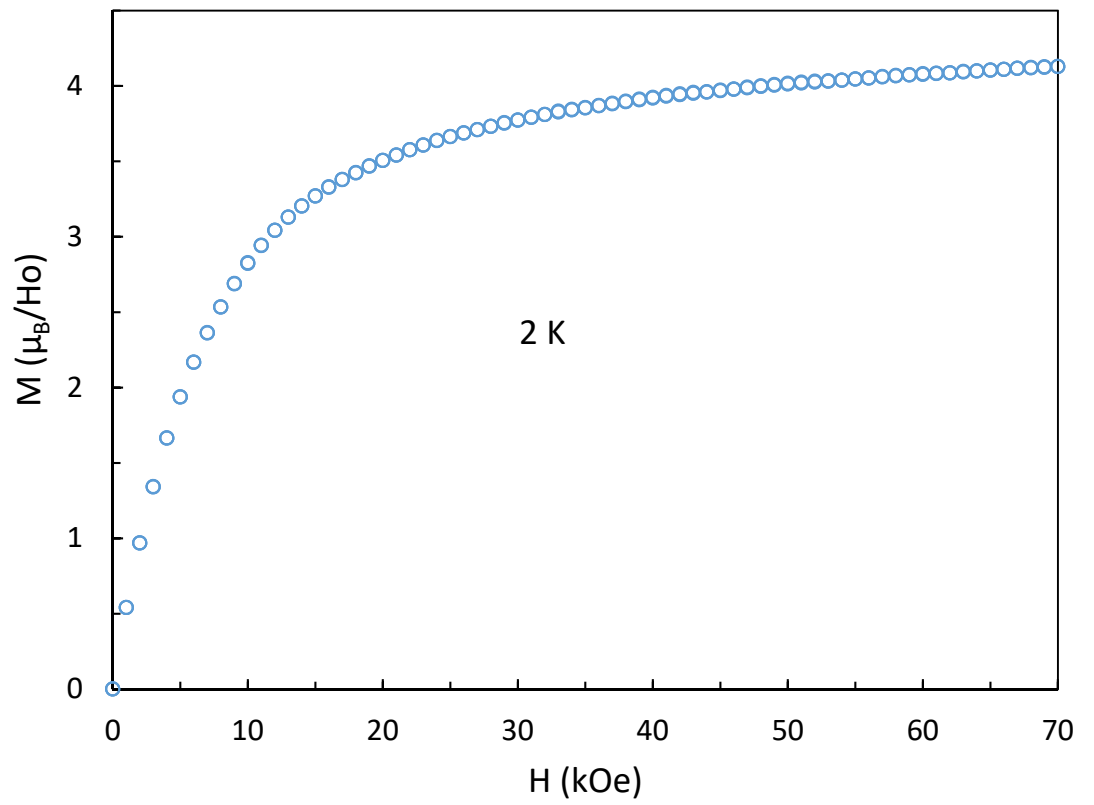
Figure 3. 12 Magnetic field dependence of magnetization of HoZn$_3$P$_3$ at 2 K.
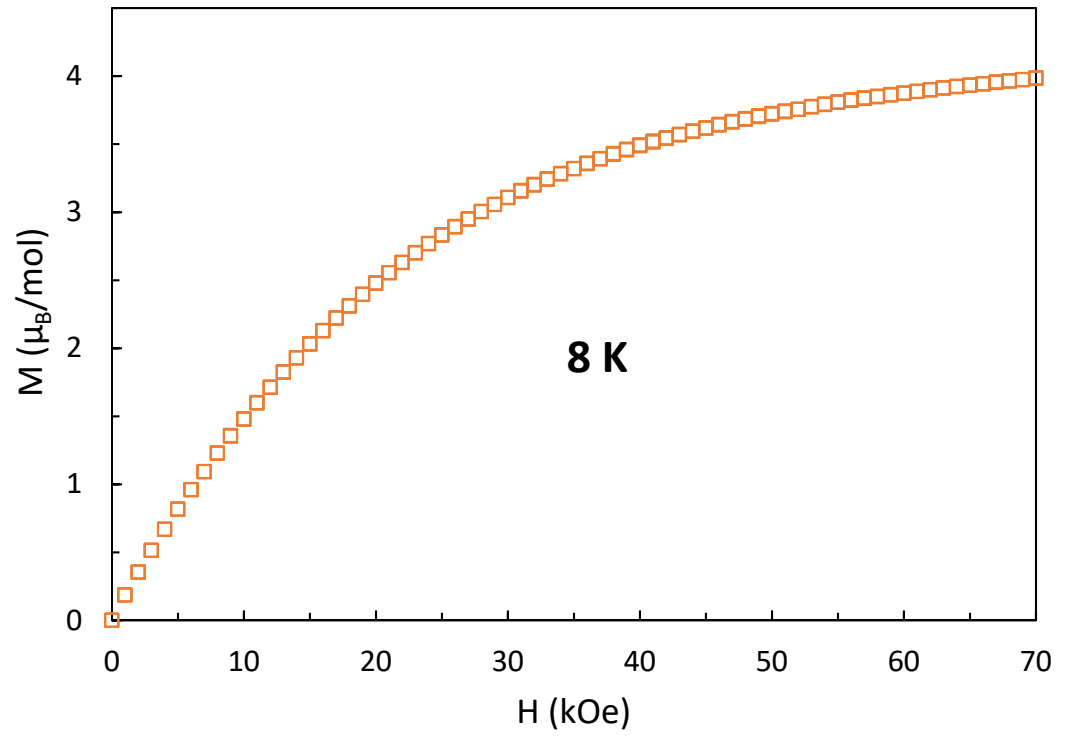
Figure 3. 13 Magnetic field dependence of magnetization of HoZn$_3$P$_3$ at 8 K.
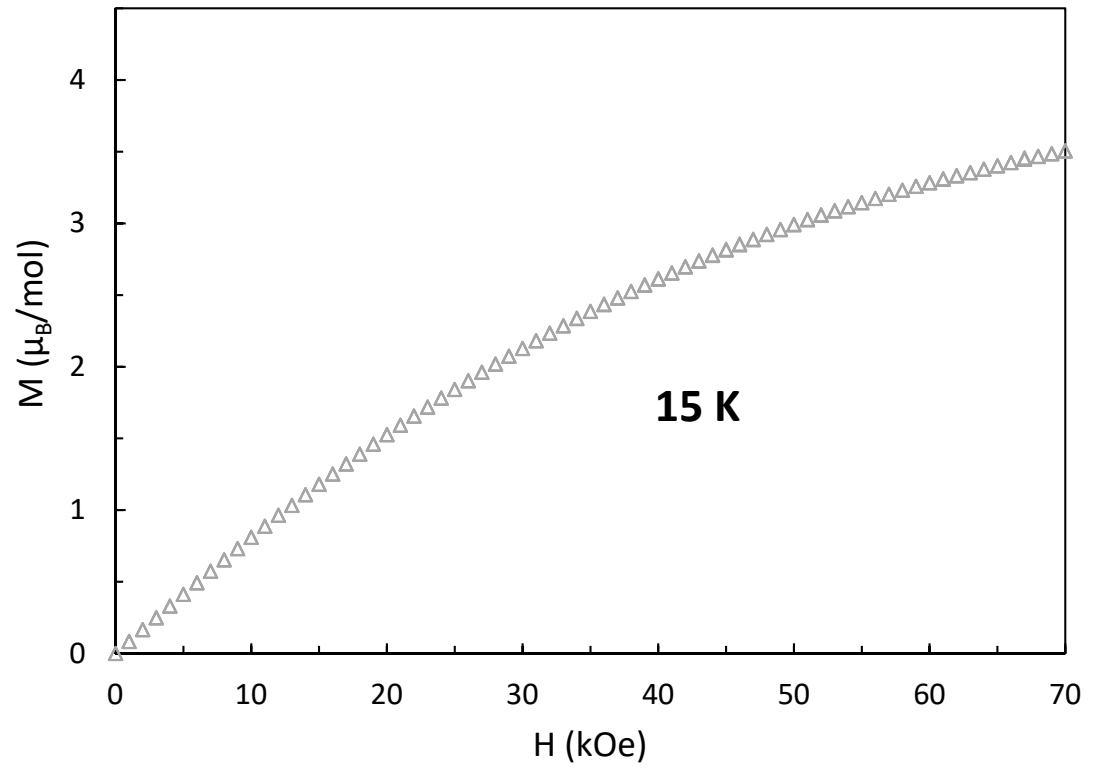
Figure 3. 14 Magnetic field dependence of magnetization of HoZn$_3$P$_3$ at 15 K.
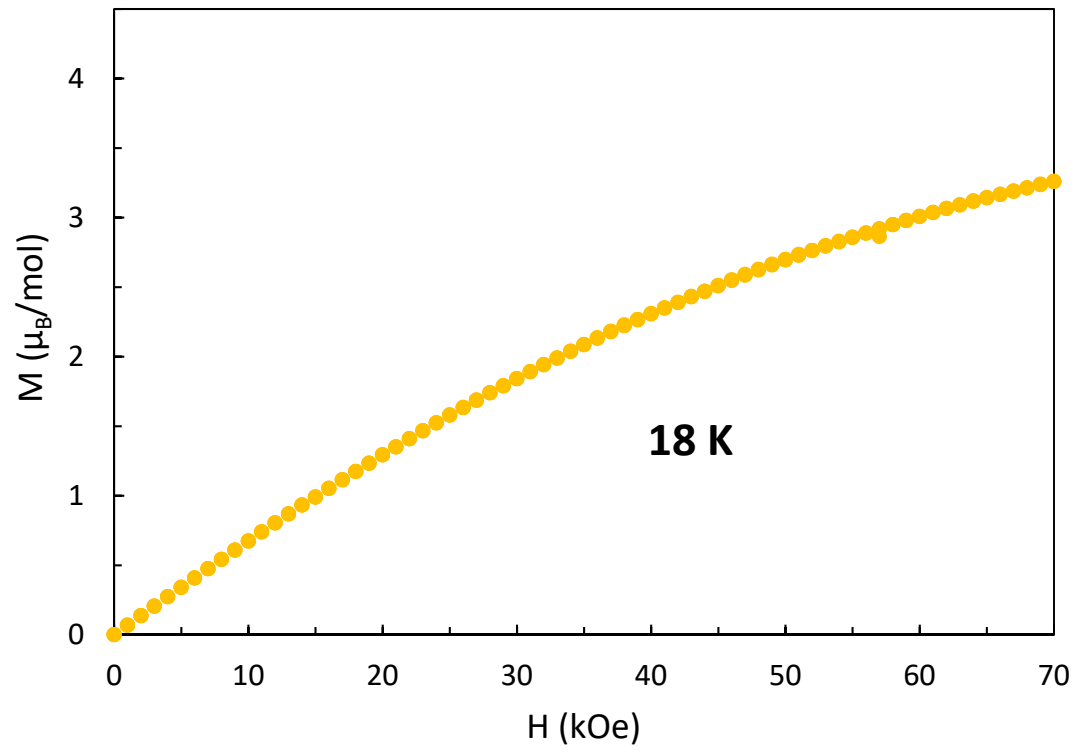
Figure 3. 15 Magnetic field dependence of magnetization of HoZn$_3$P$_3$ at 18 K.
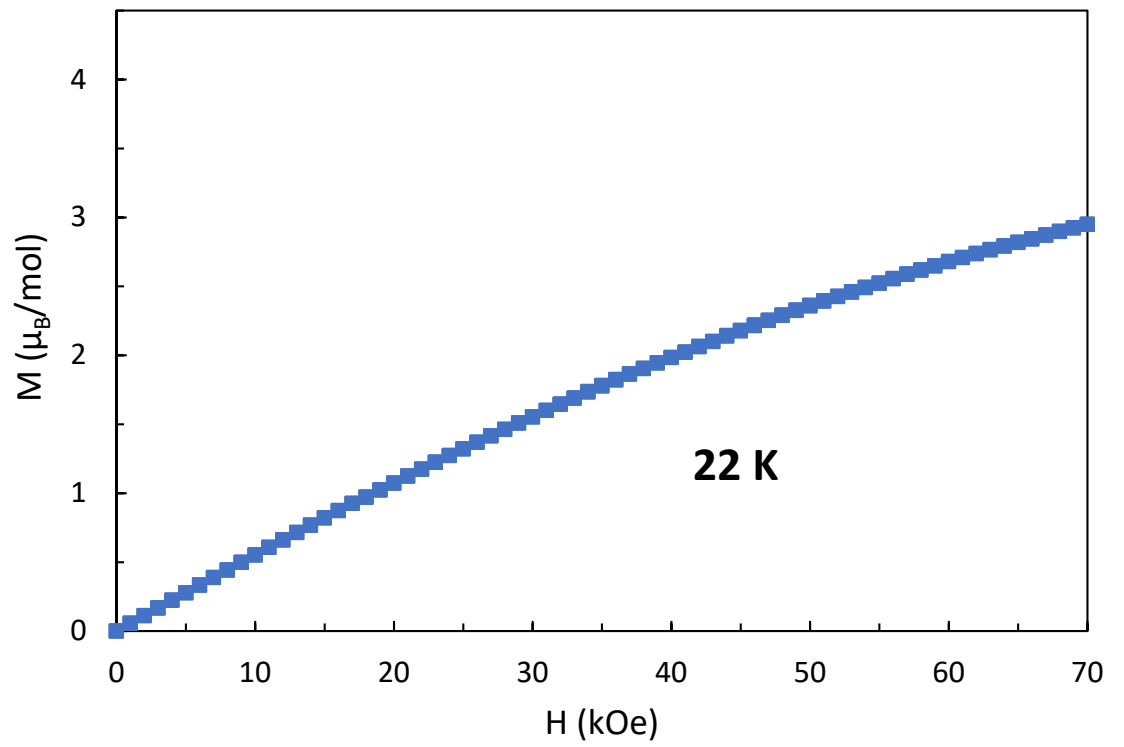
Figure 3. 16 Magnetic field dependence of magnetization of HoZn$_3$P$_3$ at 22 K.

3. 3 Specific Heat Capacity

Specific heat capacity is measured for $HoZn_3P_3$ and non-magnetic YZn_3P_3 compounds from 300 K to 2 K. Fig. 3.16 shows Specific heat as a function of temperature. The inset shows enlarged view of low temperature region. $HoZn_3P_3$ exhibits a clear kink at 4.5 K in specific heat, which corresponds to inflection point (T_M) observed in susceptibility. Magnetic heat capacity was calculated by subtracting electronic and lattice contribution to specific heat using specific heat of non-magnetic YZn_3P_3. Magnetic specific heat along with crystal field fit is shown in fig. 3.17. We assumed that broad peak around 70 K is attributed to Schottky anomaly.
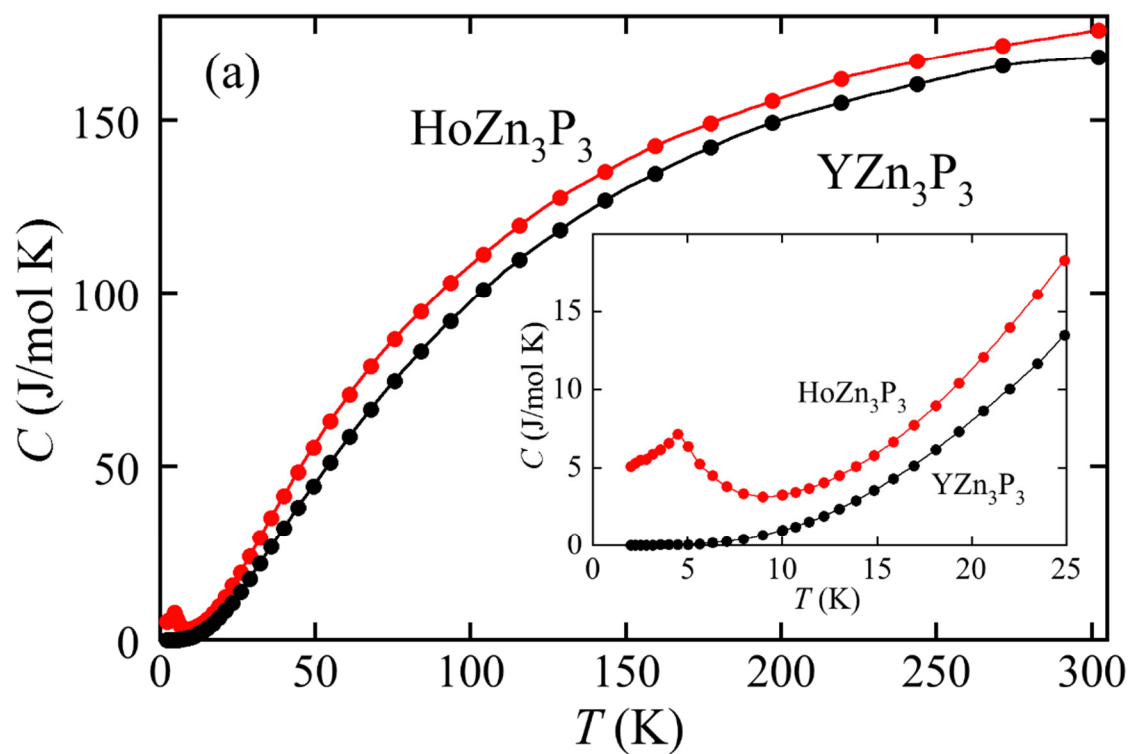
Figure 3.17 Specific heat C of HoZn$_3$P$_3$ and YZn$_3$P$_3$. Inset shows zoomed view of below 25 K.
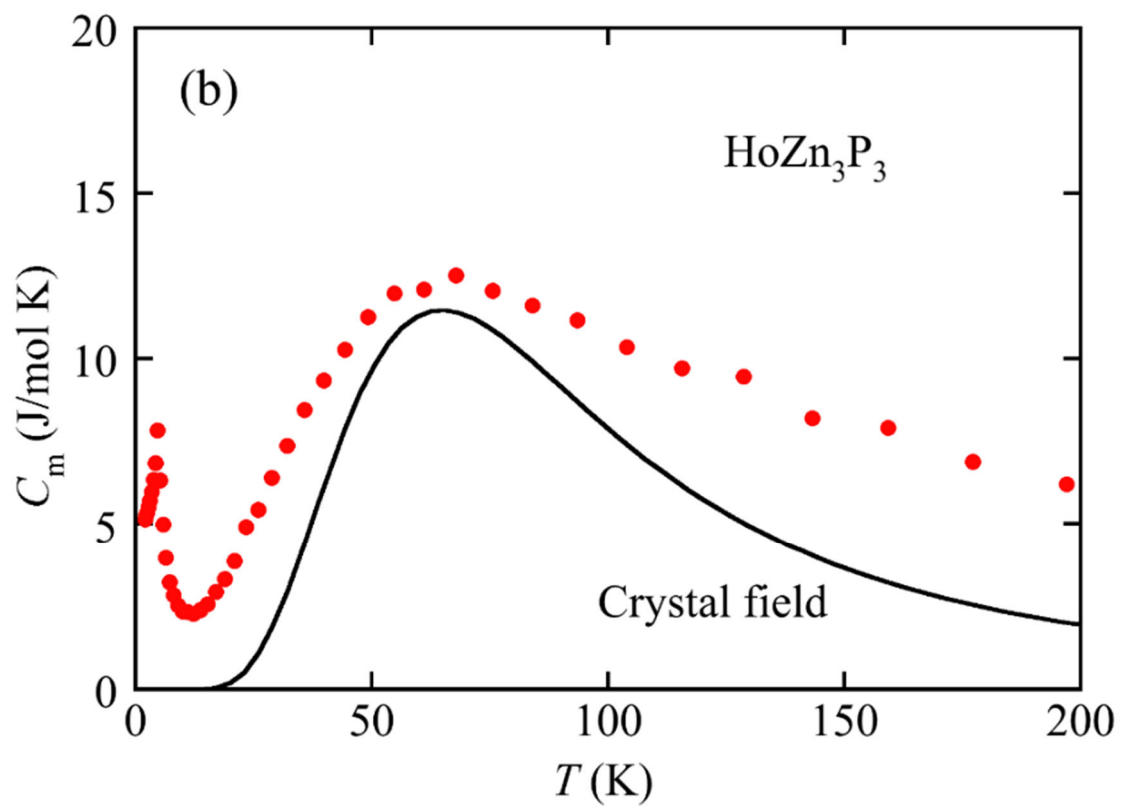
Figure 3.18 Magnetic specific heat C_m of $HoZn_3P_3$. Black solid line is a curve of CEF contribution.

Magnetic entropy S is calculated using $S = \int (C_m/T)\, dT$ from 25 K to 2 K magnetic specific heat data. Temperature dependence of the S is shown in fig. 3.18. The entropy S increases smoothly with increasing temperature and reaches 4.7 J/mol K at T_M. Hexagonal crystal electric field (CEF) potential splits the 17 degenerate levels of free Ho^{3+} ion into 6 doublets and 5 singlets. A significant entropy released at T_M suggests long range moments below T_M might be restrained by geometric frustration and Kondo effect. The fitted two level Schottky expression is given below [21],

$$C_{\text{CEF}}(T) = R \left[\frac{\sum_i g_i e^{-E_i/T} \sum_i g_i E_i^2 e^{-E_i/T} - \left[\sum_i g_i E_i e^{-E_i/T} \right]^2}{T^2 \left[\sum_i g_i e^{-E_i/T} \right]^2} \right] \quad (1)$$

Where, R is the universal gas constant, E_i is the CEF energy level function of temperature and g_i is corresponding degeneracy.

Using the equation $C = \gamma T + \beta T^3 + C_{CEF}$ where, γ is electronic specific heat coefficient, β is lattice specific heat coefficient we estimated γ and Θ_D as 199 mJ/mol K^2 and 257 K as shown in fig. 3.19. This large γ value is due to Kondo hybridization [22-26].
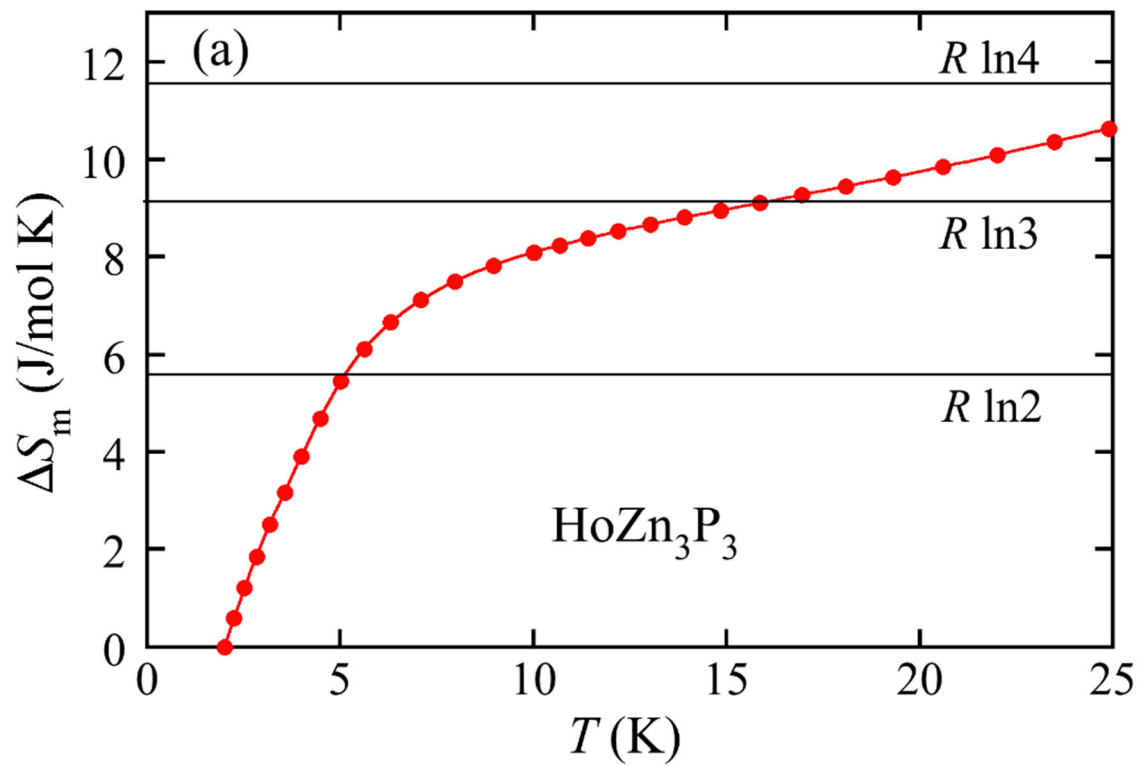
Figure 3.19 Magnetic entropy of HoZn$_3$P$_3$.
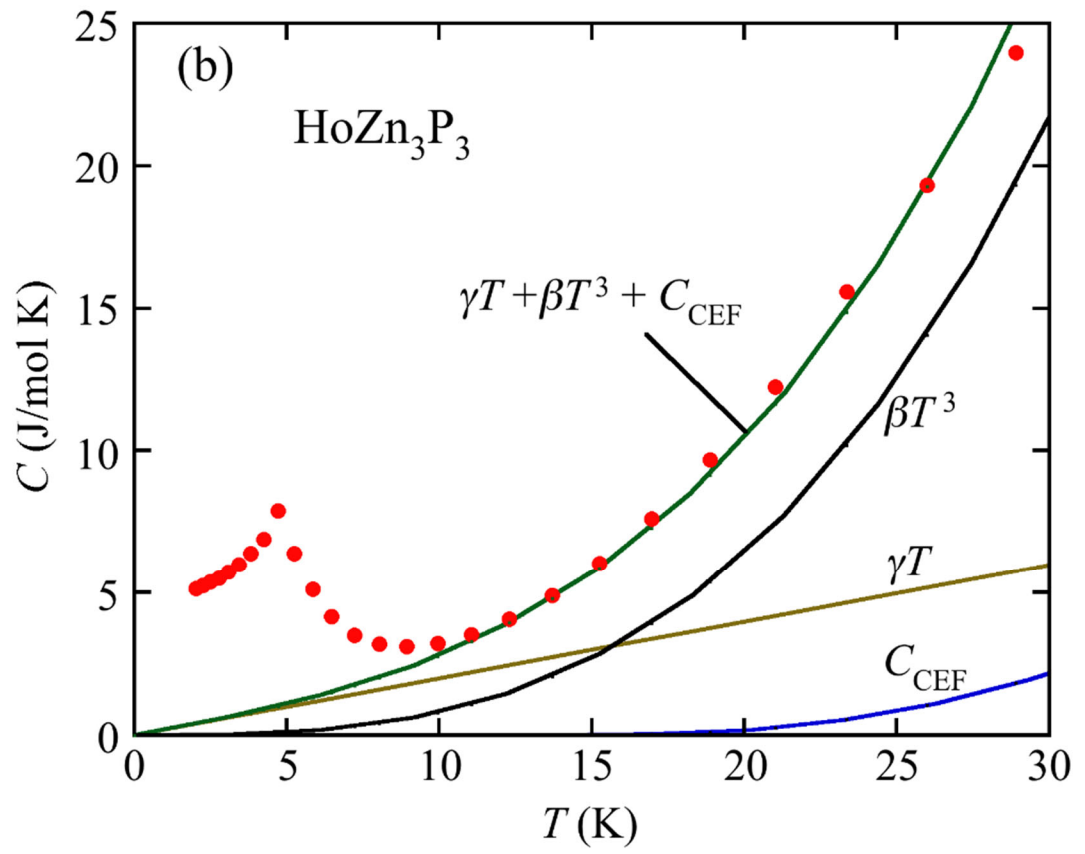
Figure 3.20 C (T) versus temperature of HoZn$_3$P$_3$ with fit.
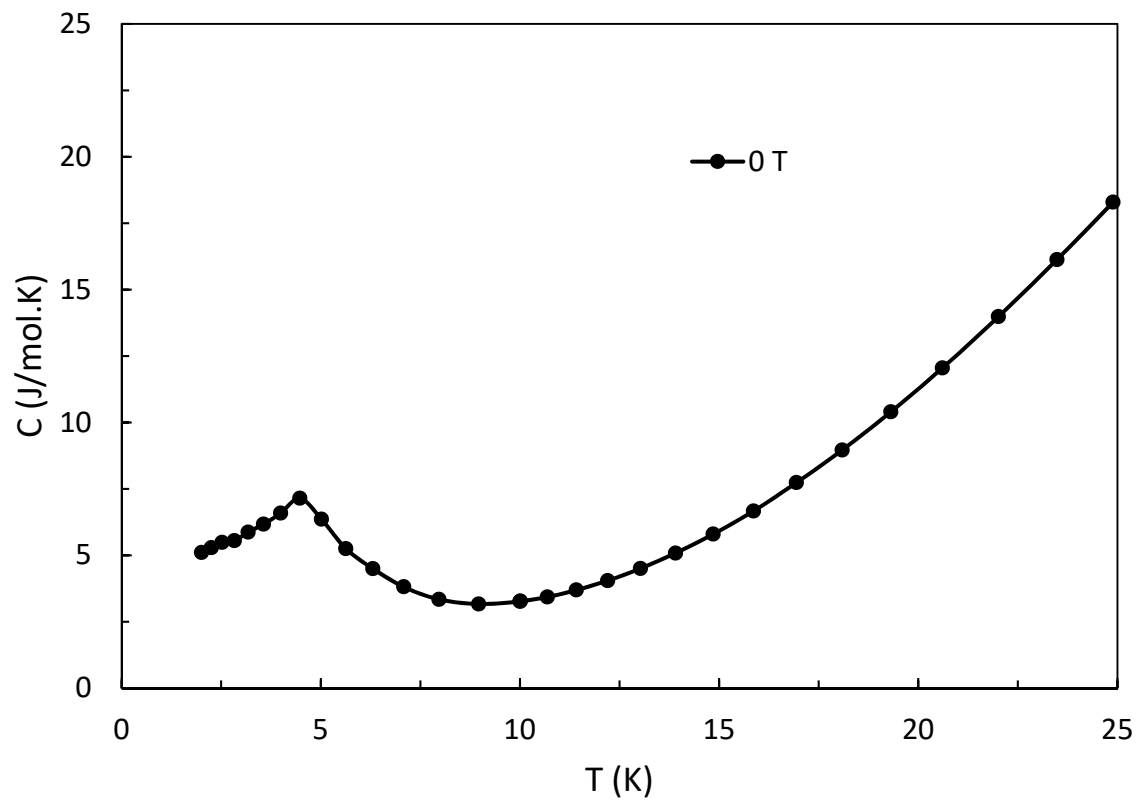
Figure 3.21 Specific heat C of HoZn$_3$P$_3$ at 0 T under 25 K.
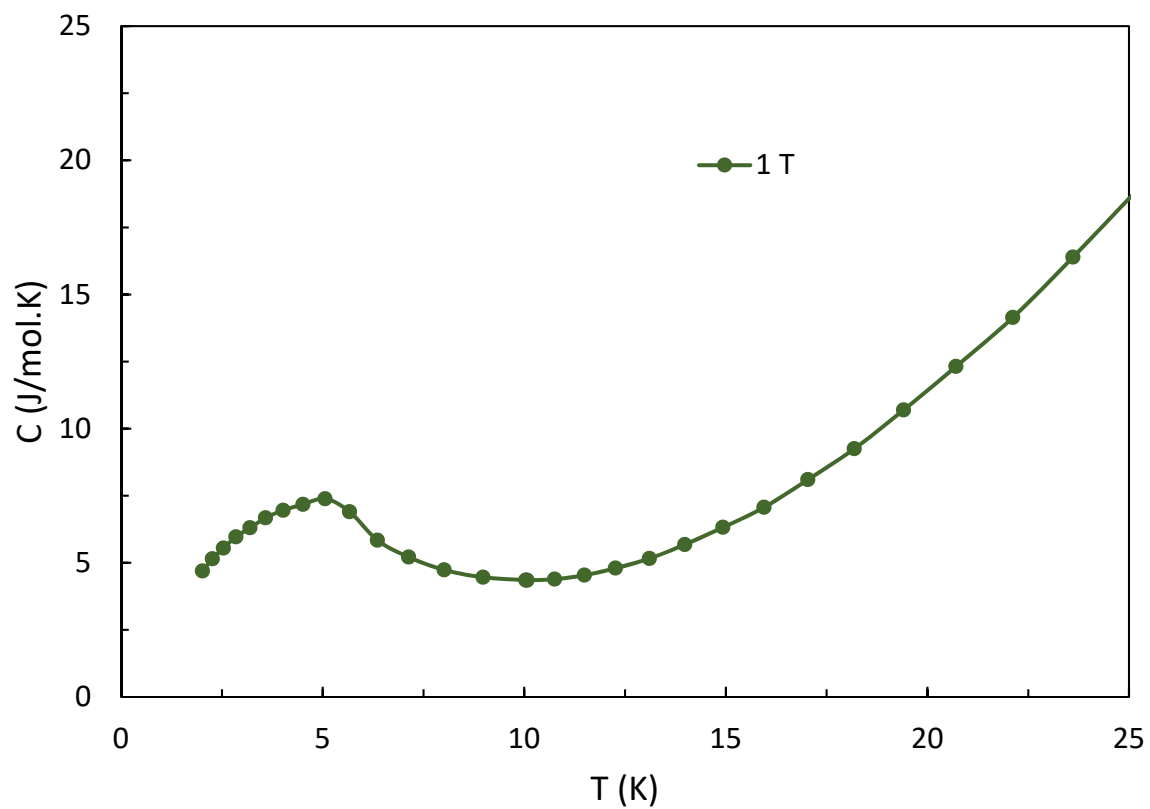
Figure 3.22 Specific heat C of HoZn$_3$P$_3$ at 1 T under 25 K.
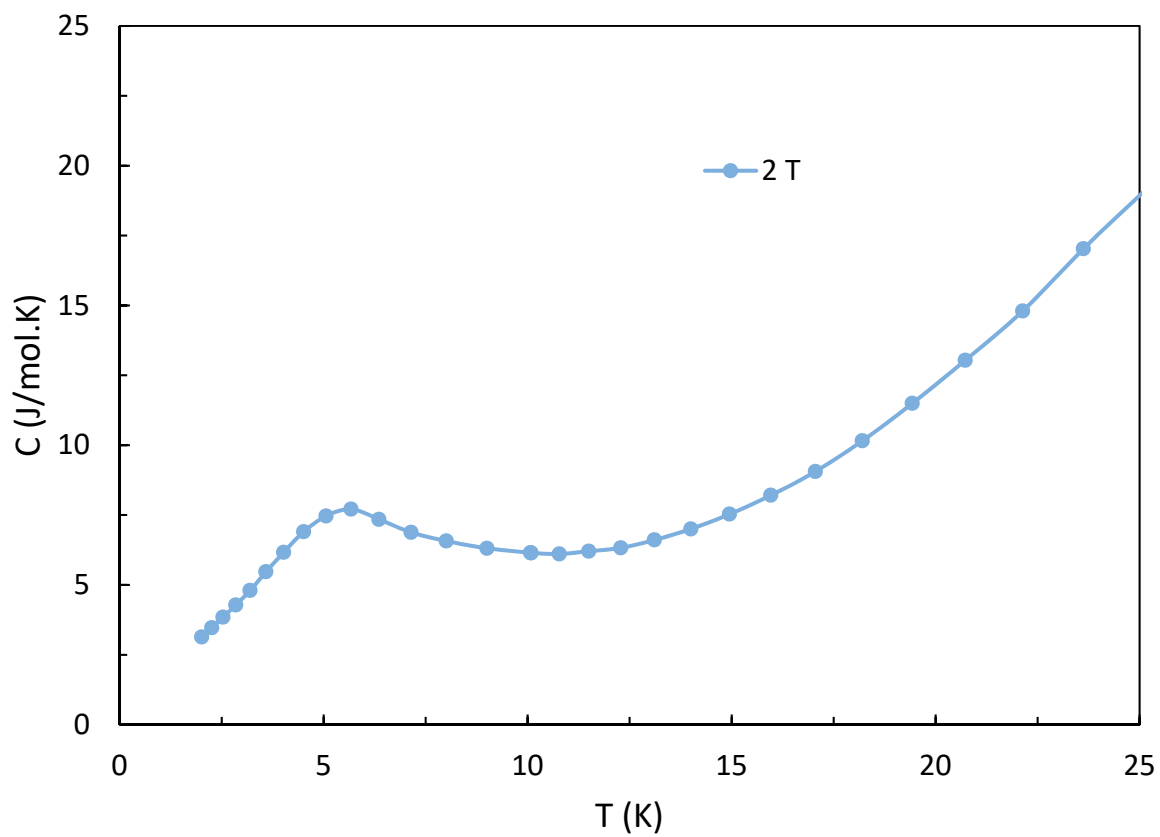
Figure 3.23 Specific heat C of HoZn$_3$P$_3$ at 2 T under 25 K.
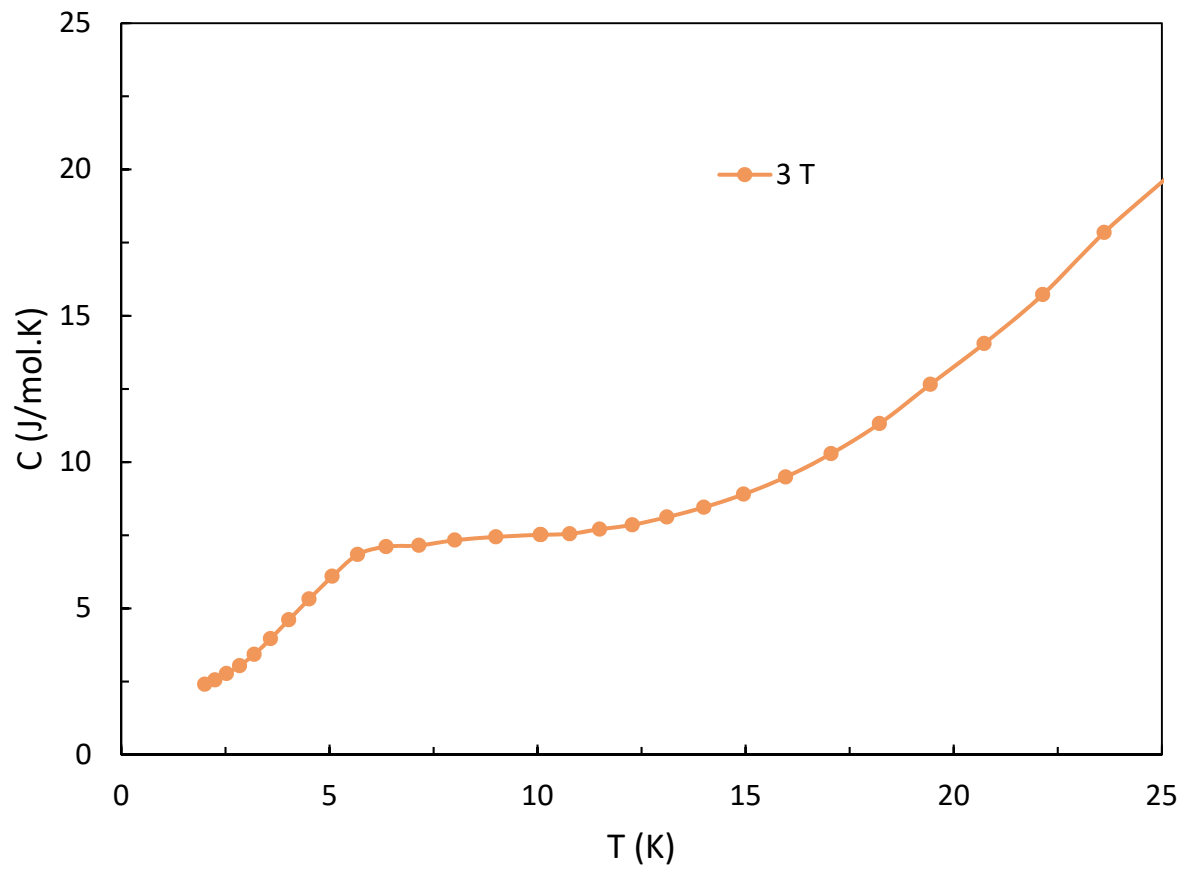
Figure 3.24 Specific heat C of HoZn$_3$P$_3$ at 3 T under 25 K.
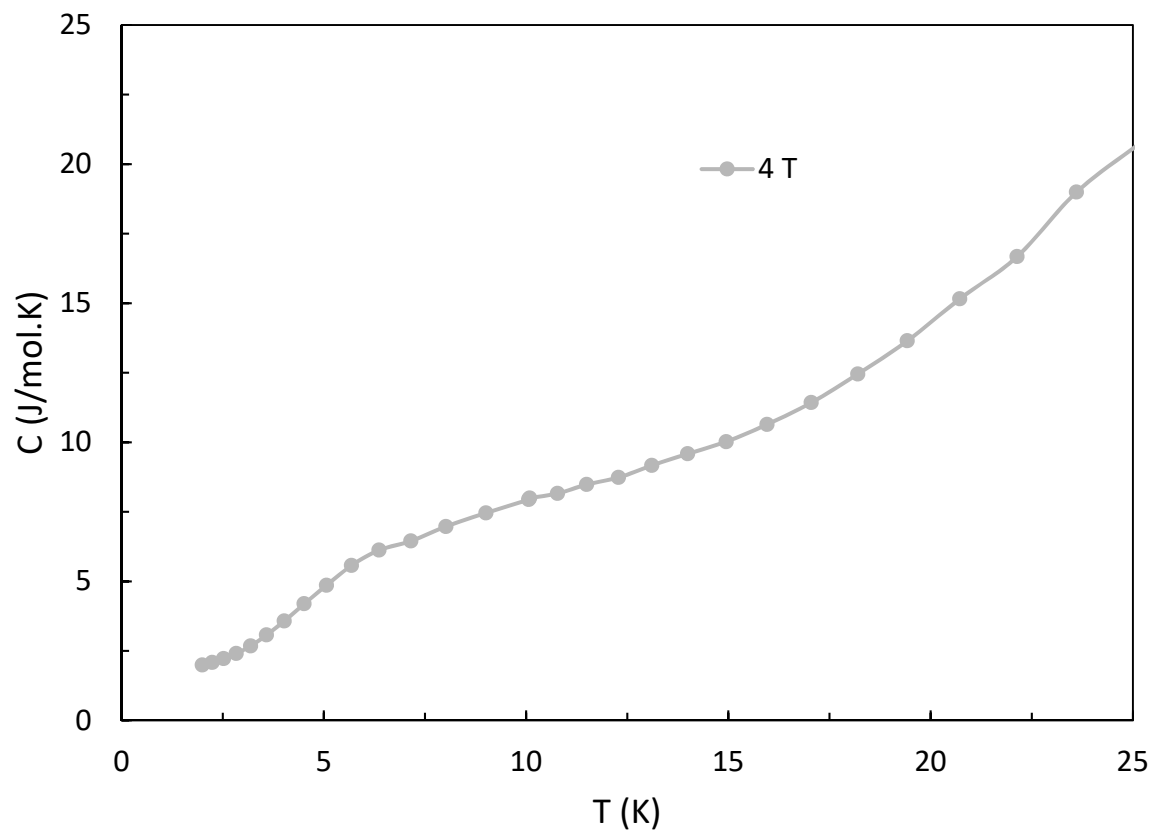
Figure 3.25 Specific heat C of HoZn$_3$P$_3$ at 4 T under 25 K.
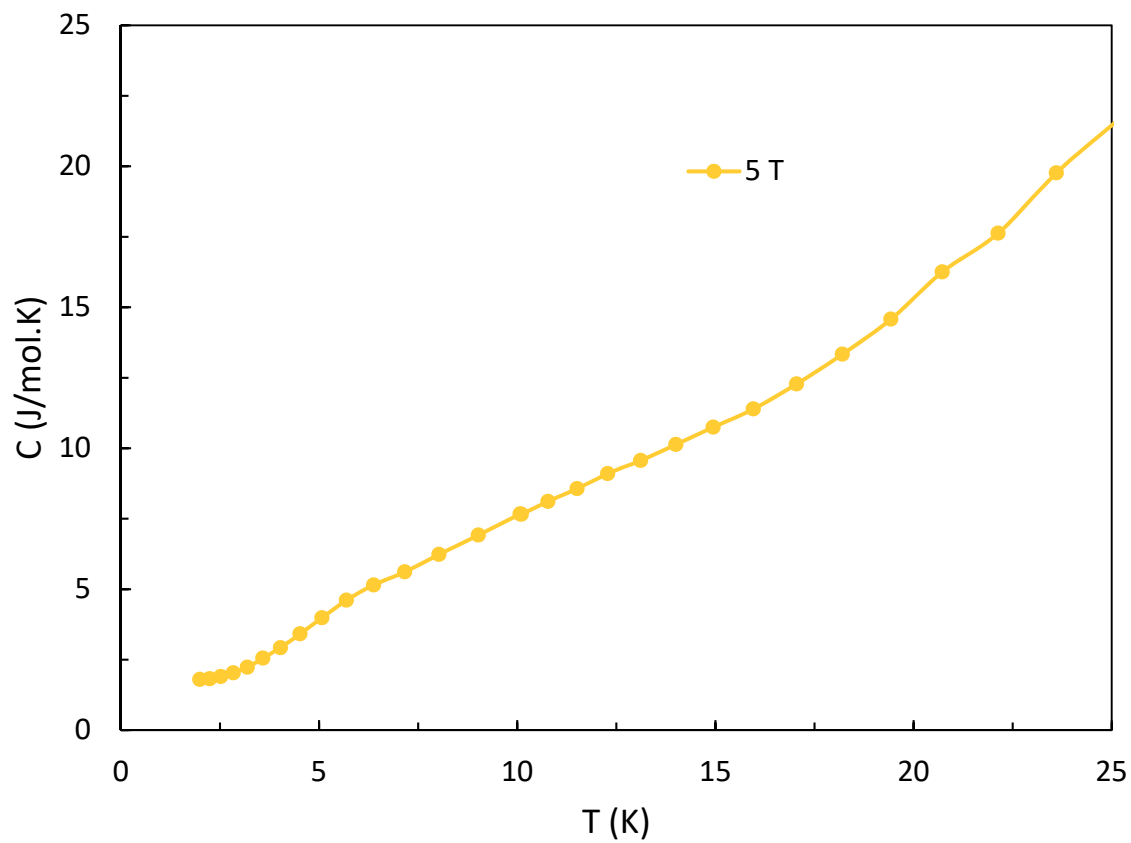
Figure 3.26 Specific heat C of HoZn$_3$P$_3$ at 5 T under 25 K.
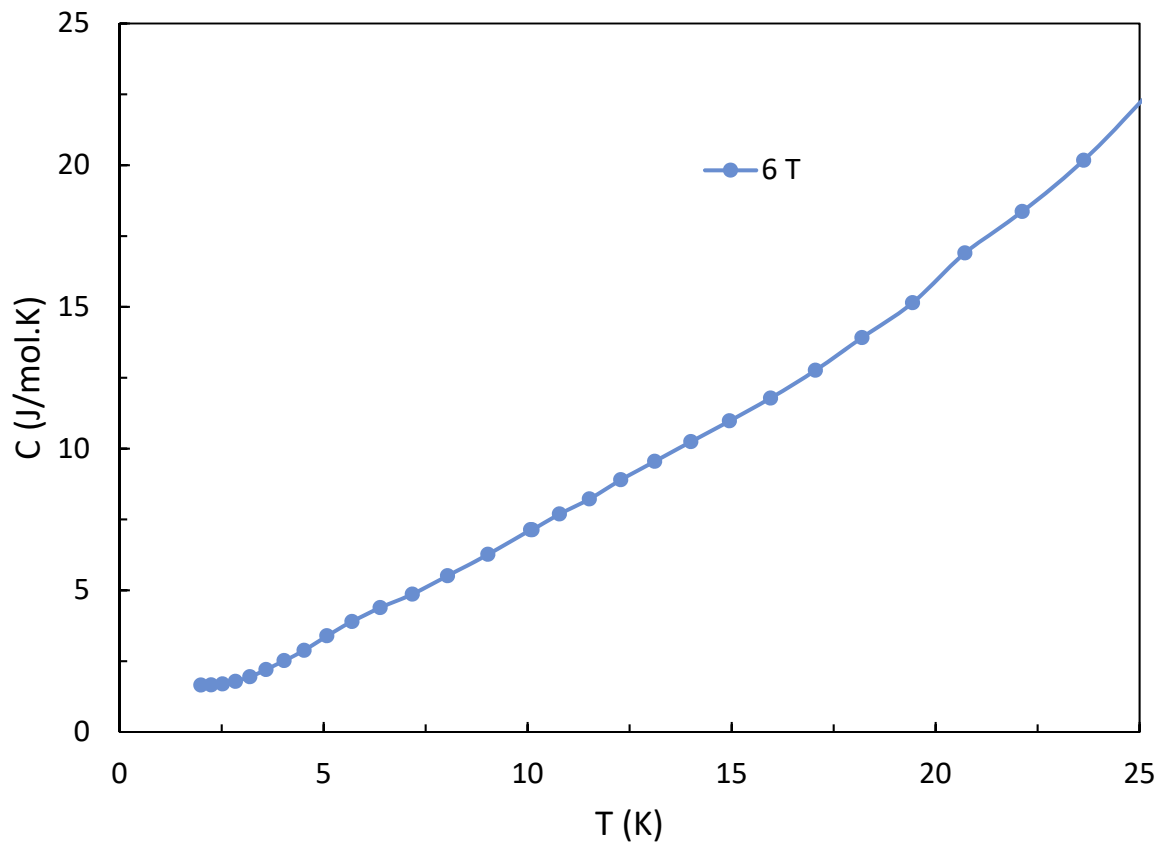
Figure 3.27 Specific heat C of $HoZn_3P_3$ at 6 T under 25 K.
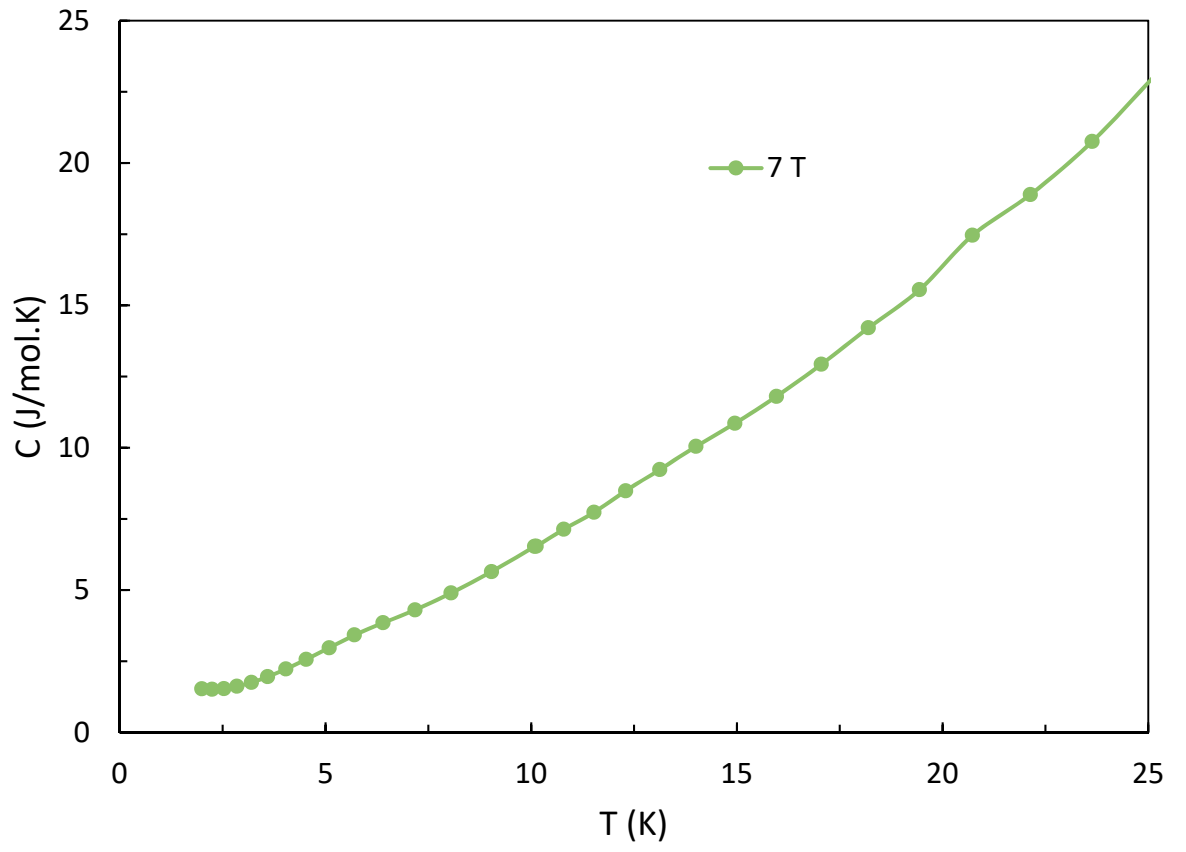
Figure 3.28 Specific heat C of HoZn$_3$P$_3$ at 7 T under 25 K.

As magnetic field increases the kink shifts towards high temperature region which can be seen from fig. 3.20-3.27. The kink disappears above 30 kOe. The magnetic field dependence of γ value is calculated and shown in fig. 3.28. The γ value increases as field increases and reaches maximum of 660 mJ/mol K^2 at 60 kOe. Above 60 kOe, it starts decrease. Using the results of specific heat capacity data under magnetic field, we constructed the partial *H-T* phase diagram which is shown in fig. 3.29.
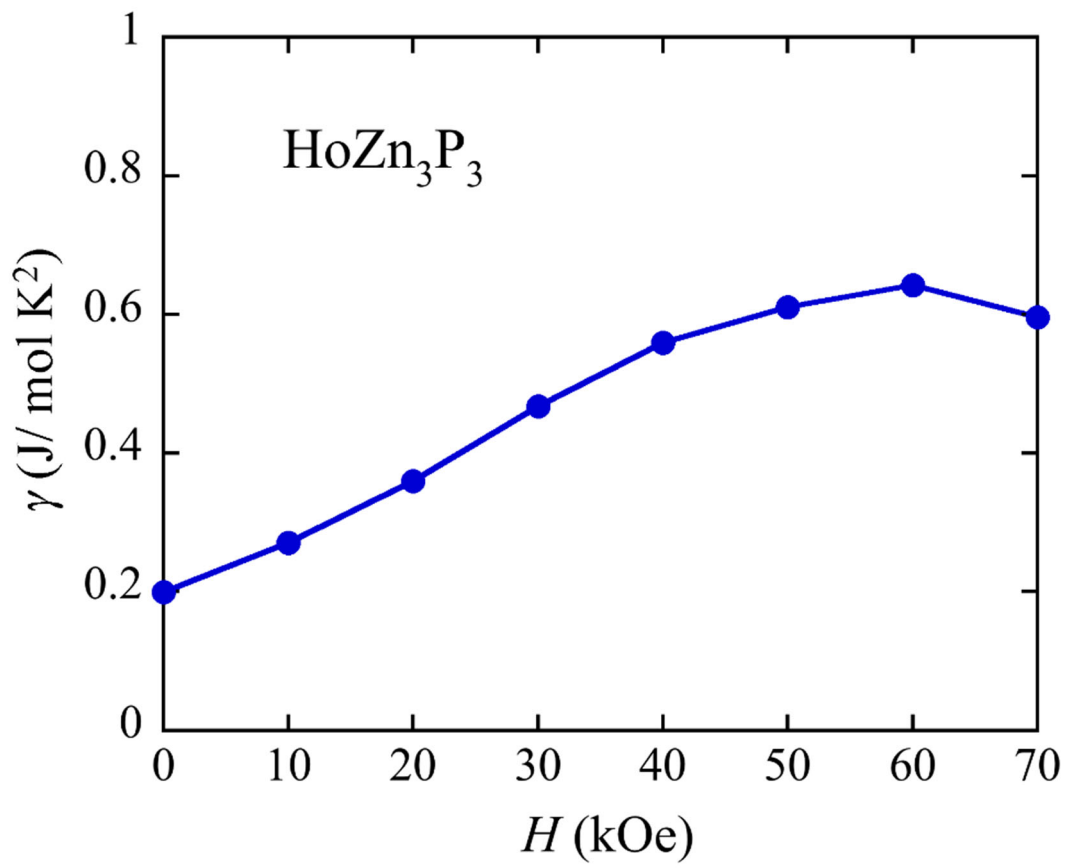
Figure 3.29 shows γ value versus applied magnetic field H (kOe).
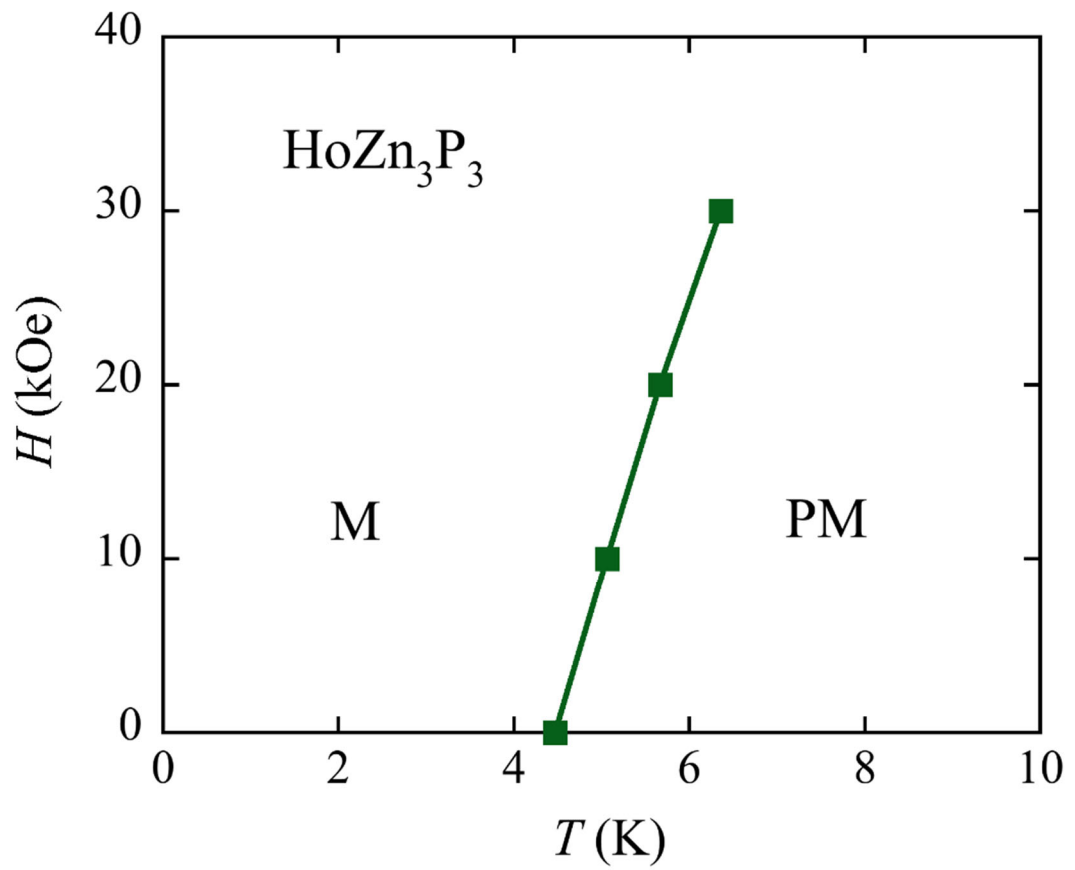
Figure 3.30 Phase diagram of HoZn₃P₃. M denotes the magnetic region and PM denotes the paramagnetic region. Solid line is to guide to eyes.

3.4 Electrical resistivity

$HoZn_3P_3$ exhibits a metallic behaviour at high temperature and displays a minimum at 17 K (T_{min}). Resistivity starts to increase below T_{min} and reaches low temperature maximum at 4. 5 K (T_{max}) which can be seen in fig. 3.30 and 3.31. Room temperature resistivity value is large compared to typical metals. Resistivity of YZn_3P_3 is shown in fig. 3.32. Electrical resistivity of YZn_3P_3 exhibits metallic nature. Resistivity of YZn_3P_3 decreases with decreasing temperature. Resistivity upturn caused by Kondo interaction follows negative logarithmic temperature dependency (-log T) [27][28]. Hence, we plotted the magnetic resistivity versus temperature using resistivity value under 70 kOe. Resistivity upturn follows - log T which is due to Kondo effect along with other contribution as shown in fig. 3.40 - 42. Kondo interaction occurs when localized f electrons interact with conduction electrons. The resistivity upturn is suppressed under high magnetic field (H = 20 kOe) and follows metallic under high magnetic field as shown in fig. 3.32-3.39.
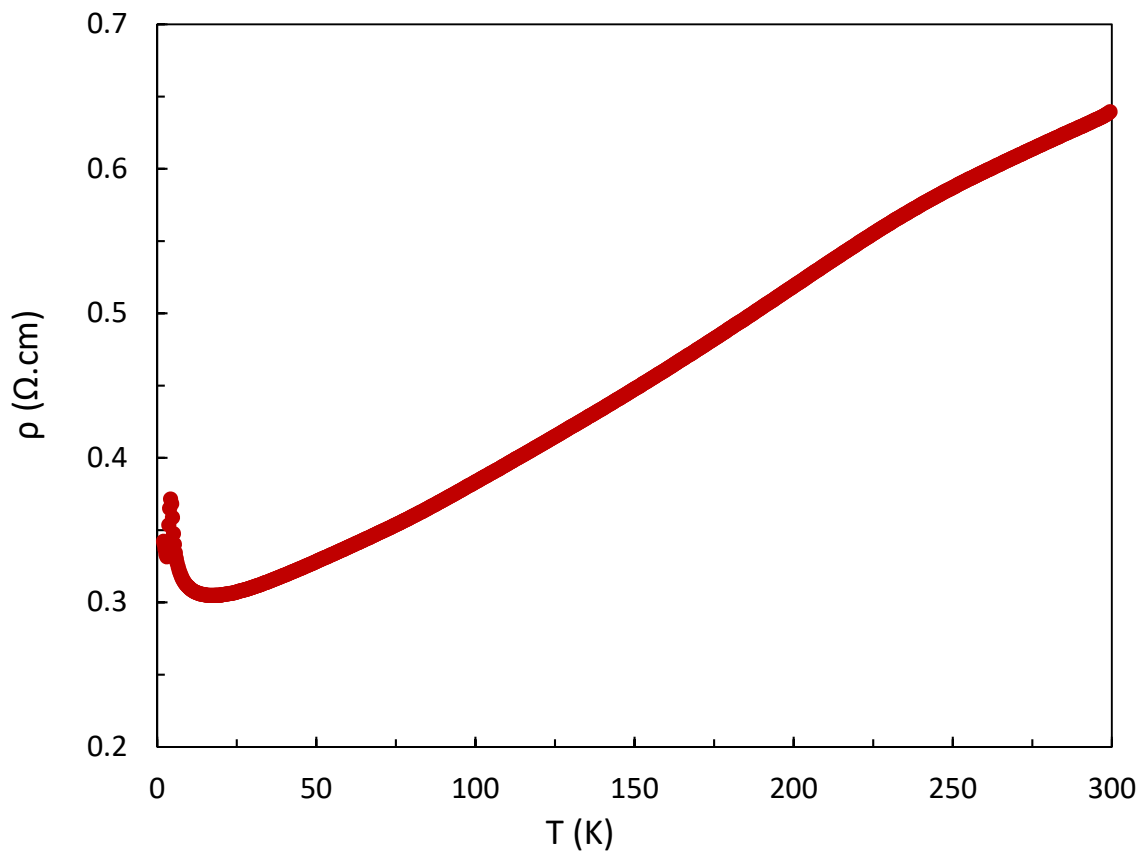
Figure 3.31 Temperature dependence of electrical resistivity of HoZn$_3$P$_3$.
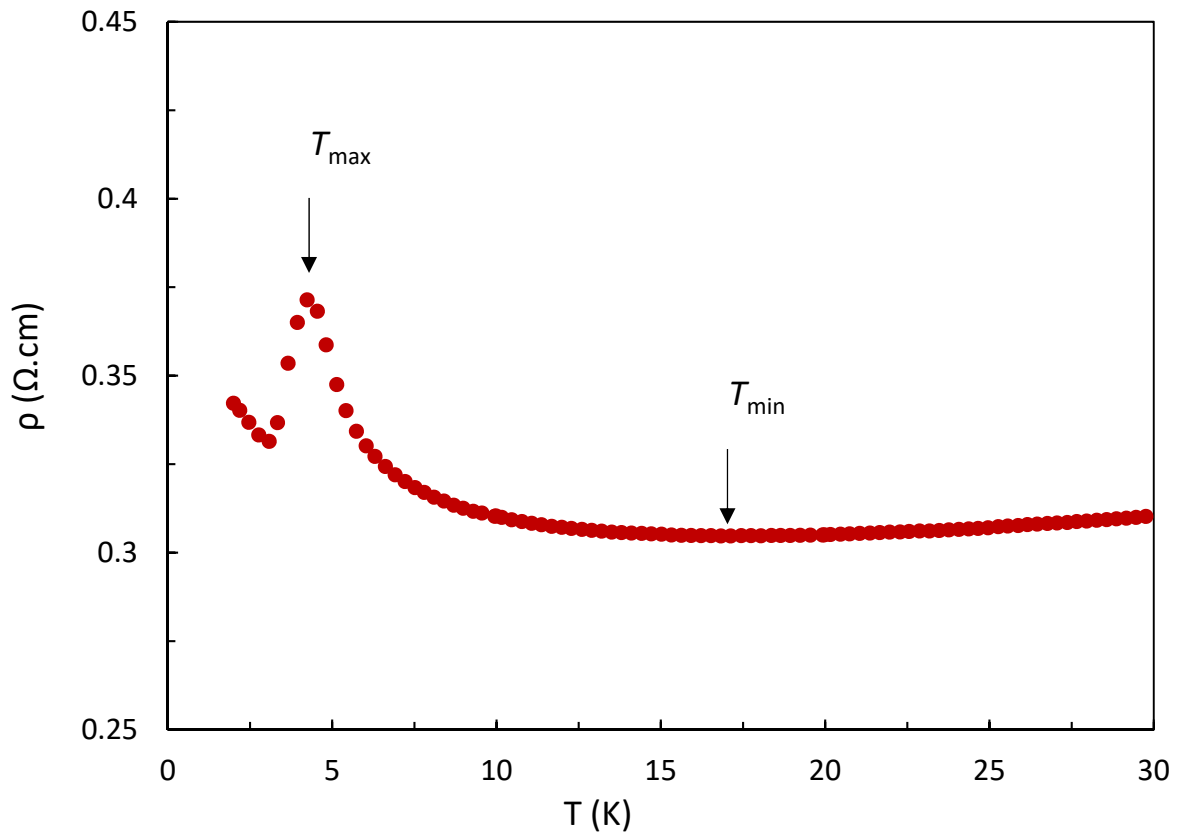
Figure 3.32 Temperature dependence of electrical resistivity of HoZn$_3$P$_3$ at low temperature.
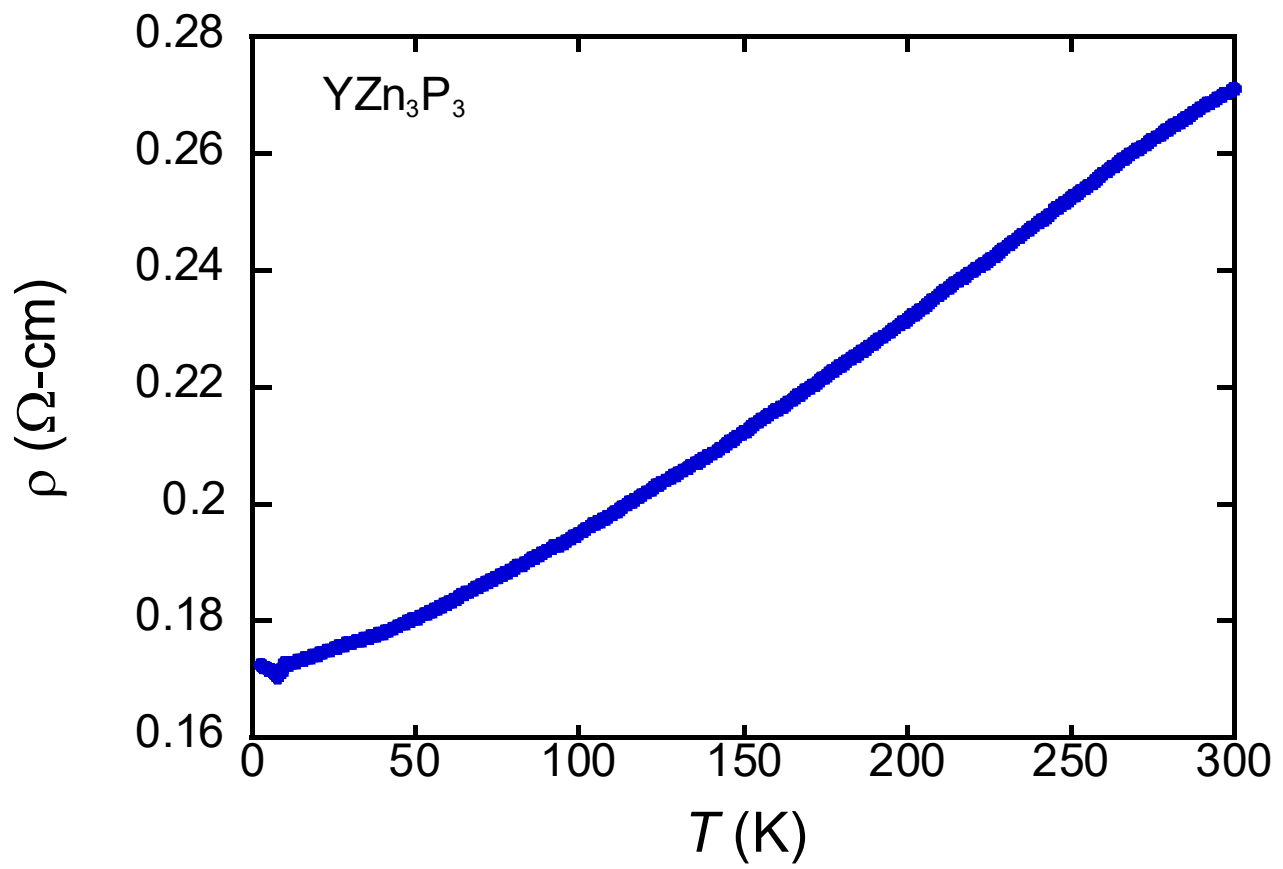
Figure 3.33 Temperature dependence of electrical resistivity of HoZn$_3$P$_3$.
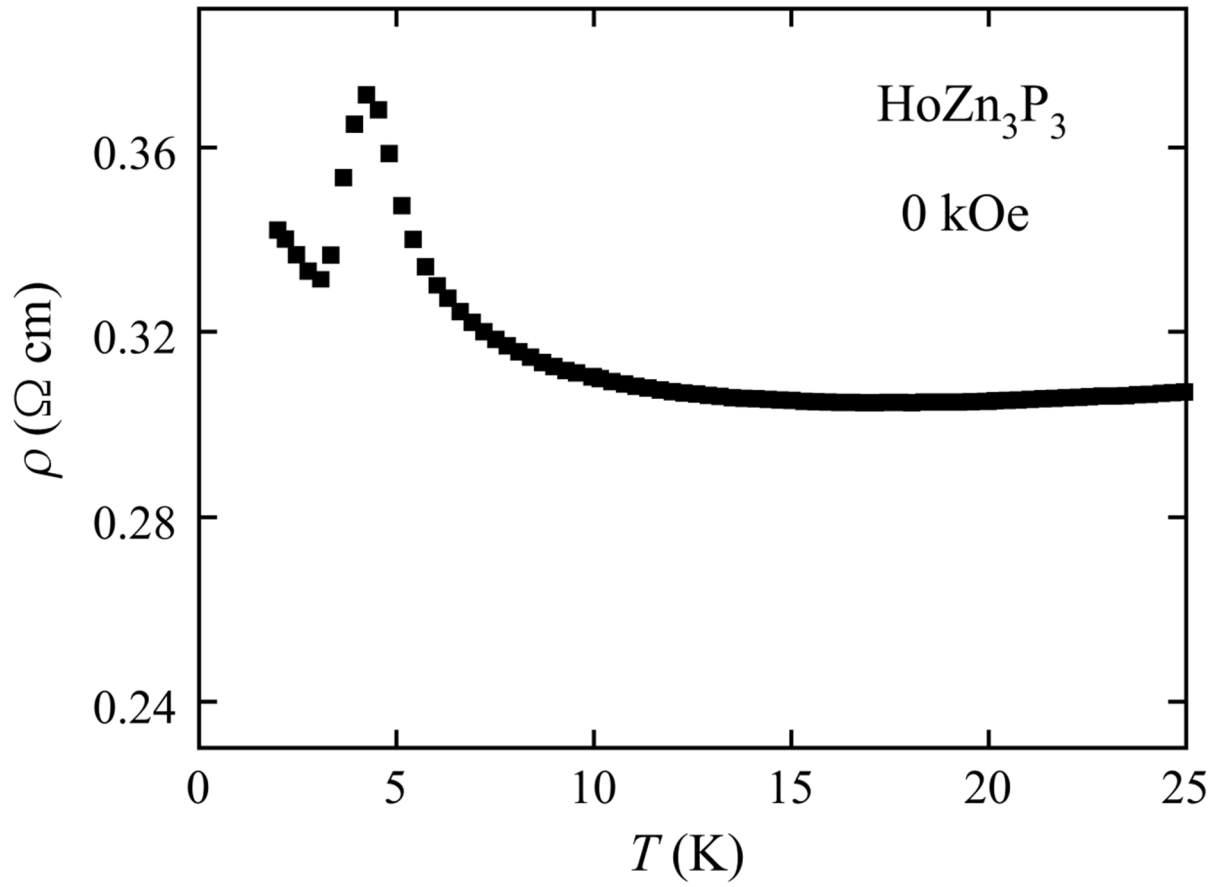
Figure 3.34 Temperature dependence of electrical resistivity of HoZn₃P₃ at 0 kOe below 25 K.
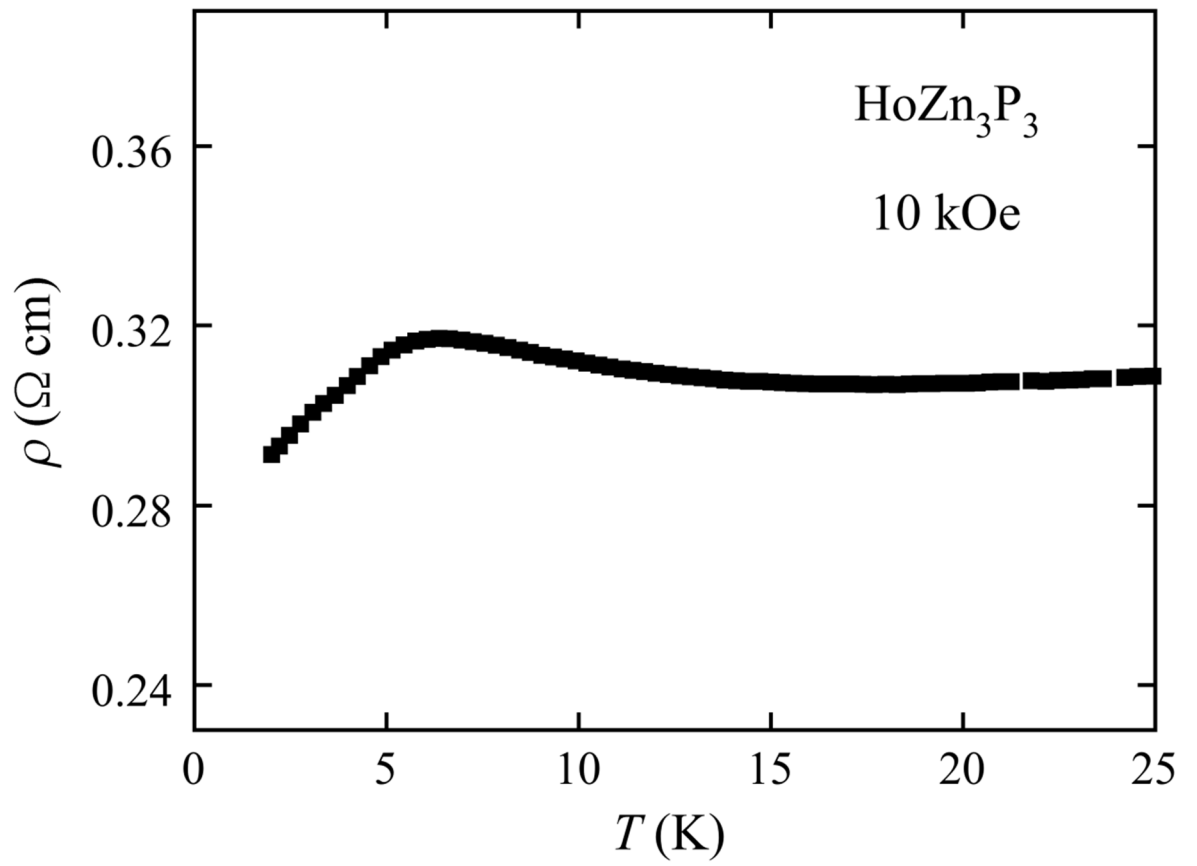
Figure 3.35 Temperature dependence of electrical resistivity of HoZn$_3$P$_3$ at 10 kOe below 25 K.
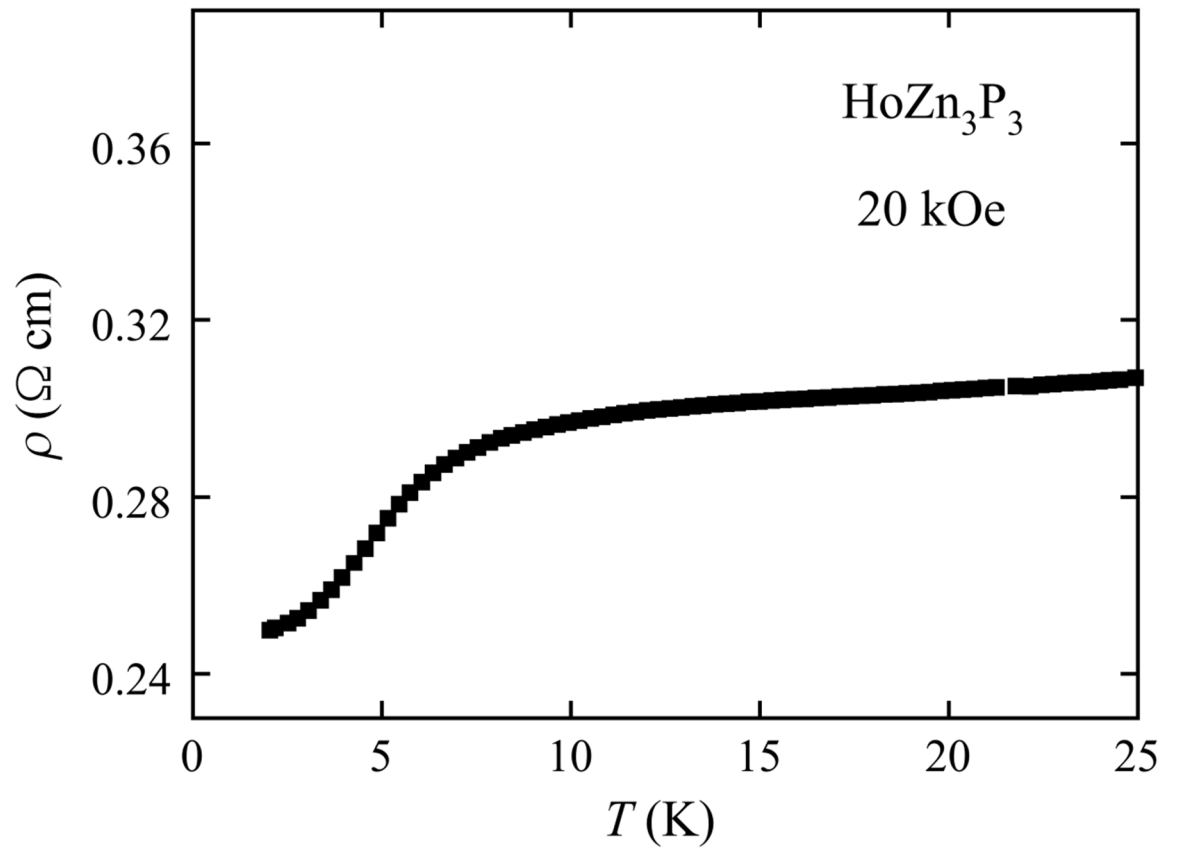
Figure 3.36 Temperature dependence of electrical resistivity of HoZn$_3$P$_3$ at 20 kOe below 25 K.
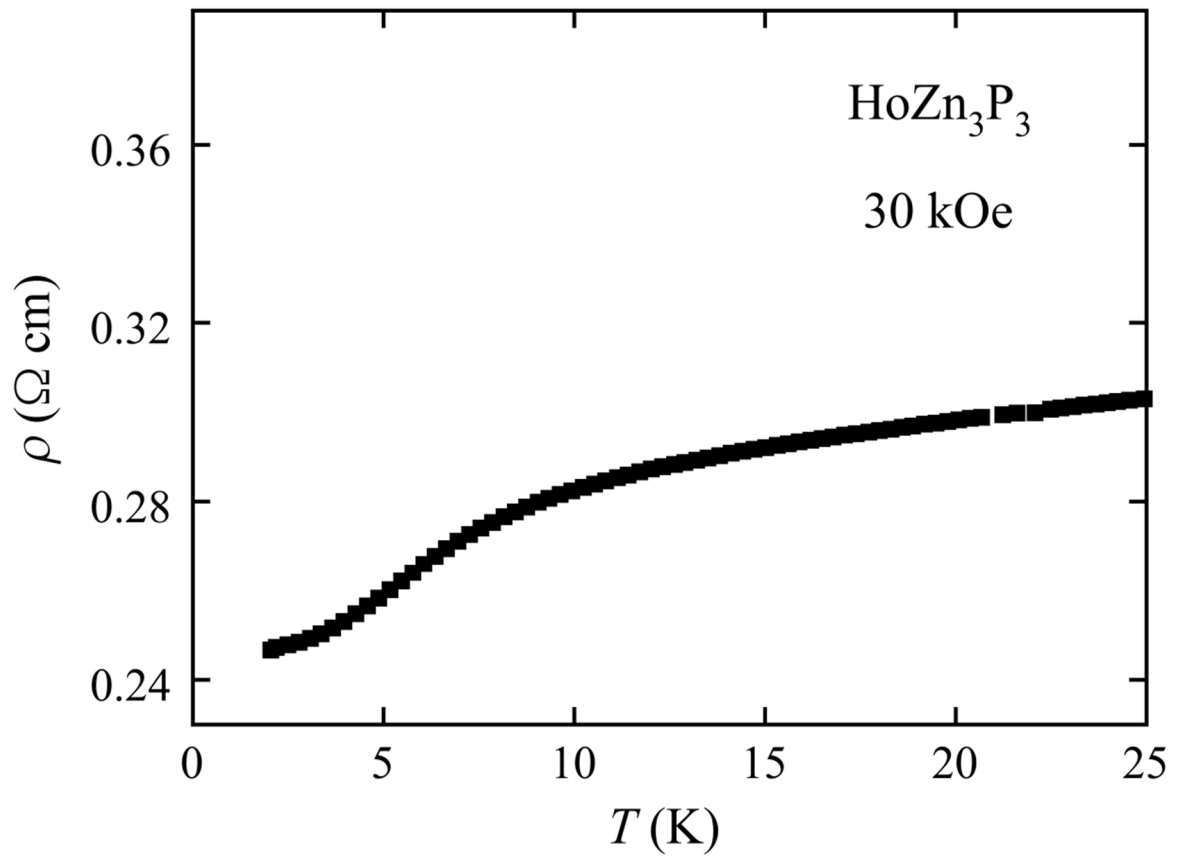
Figure 3.37 Temperature dependence of electrical resistivity of HoZn$_3$P$_3$ at 30 kOe below 25 K.
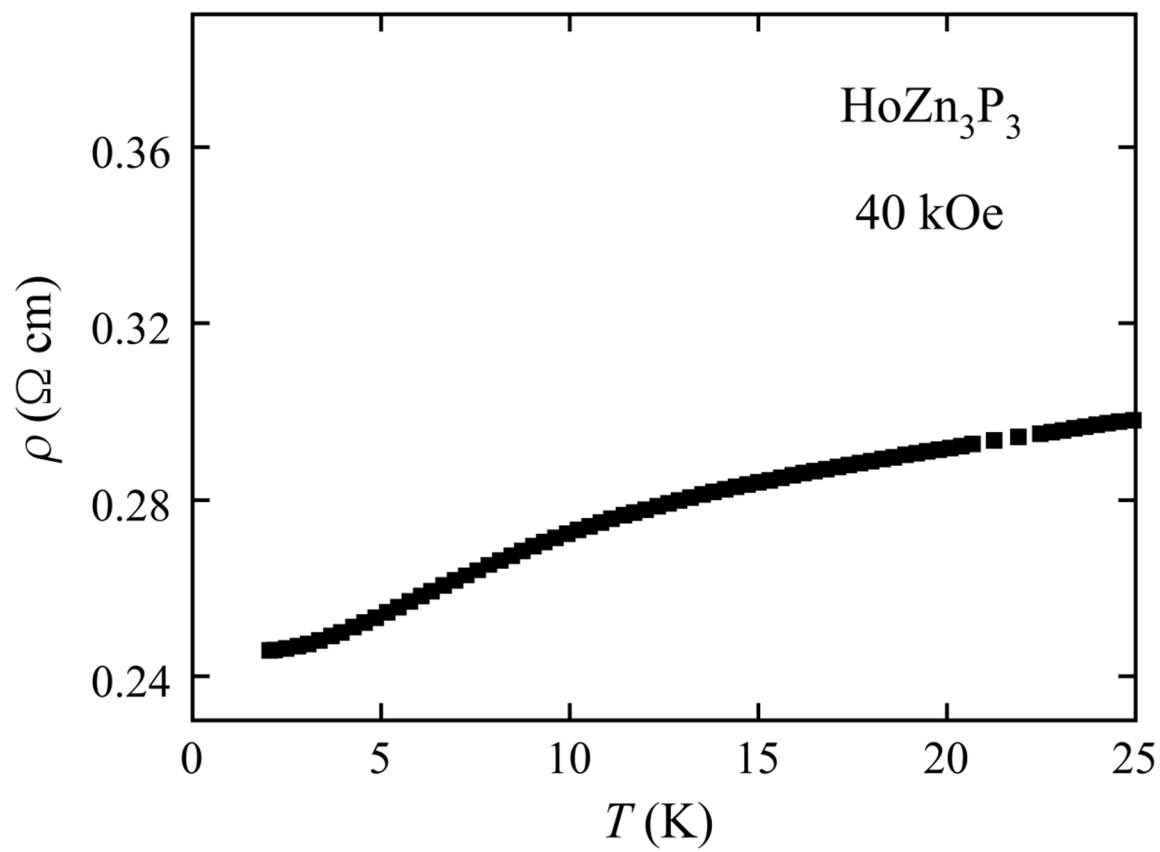
Figure 3.38 Temperature dependence of electrical resistivity of HoZn$_3$P$_3$ at 40 kOe below 25 K.
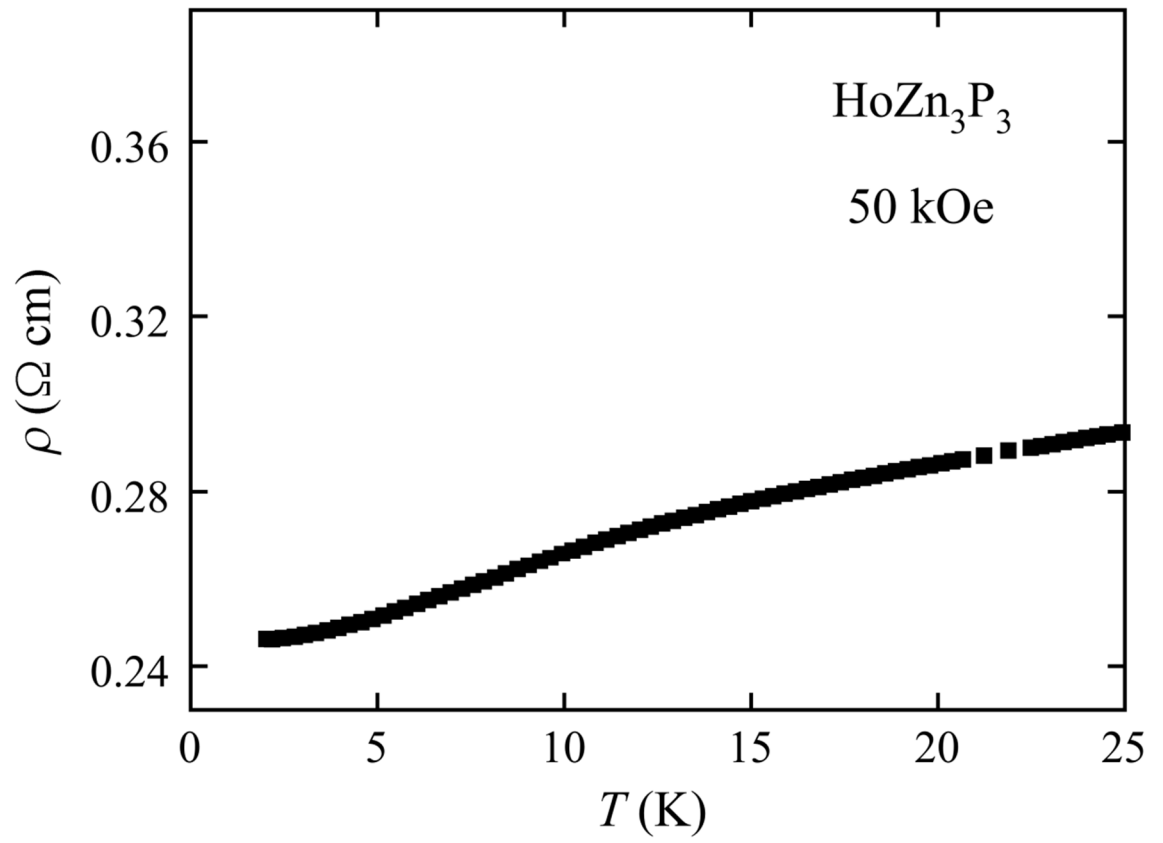
Figure 3.39 Temperature dependence of electrical resistivity of HoZn$_3$P$_3$ at 50 kOe below 25 K.
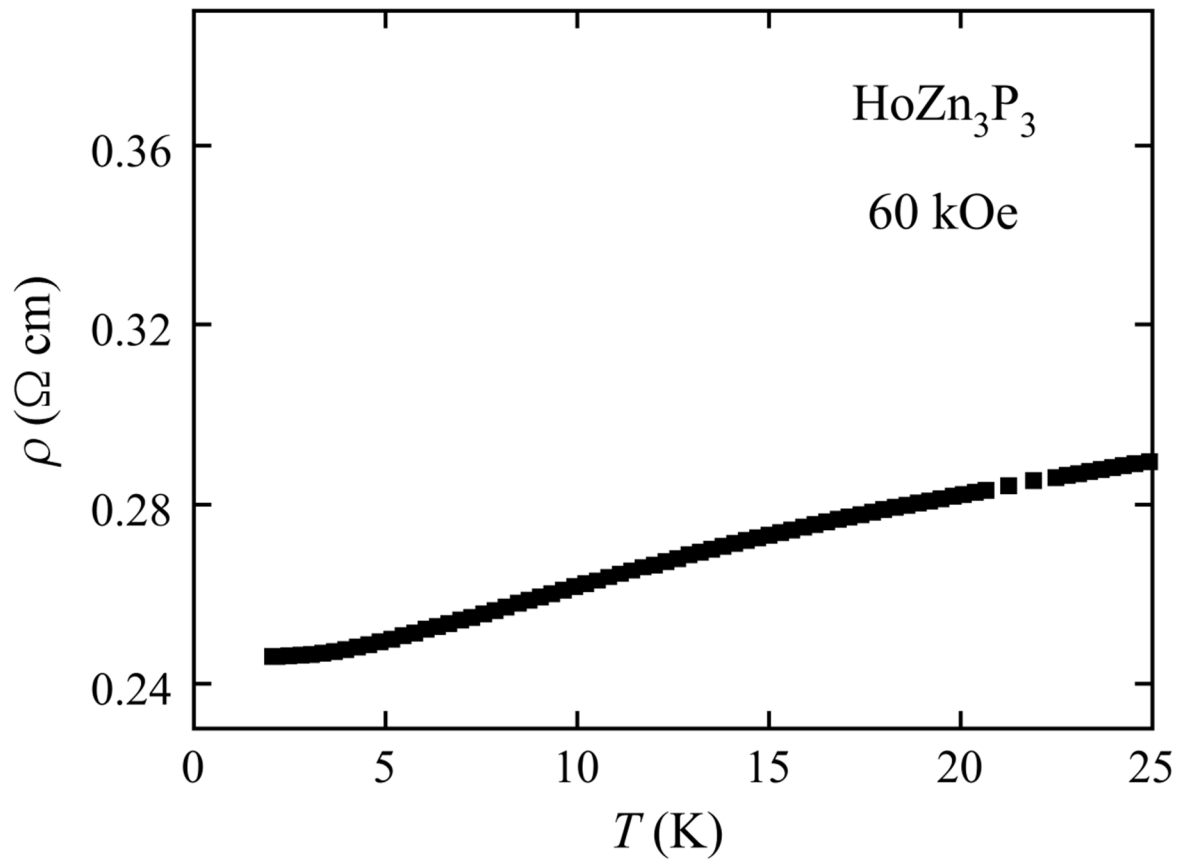
Figure 3.40 Temperature dependence of electrical resistivity of HoZn₃P₃ at 60 kOe below 25 K.
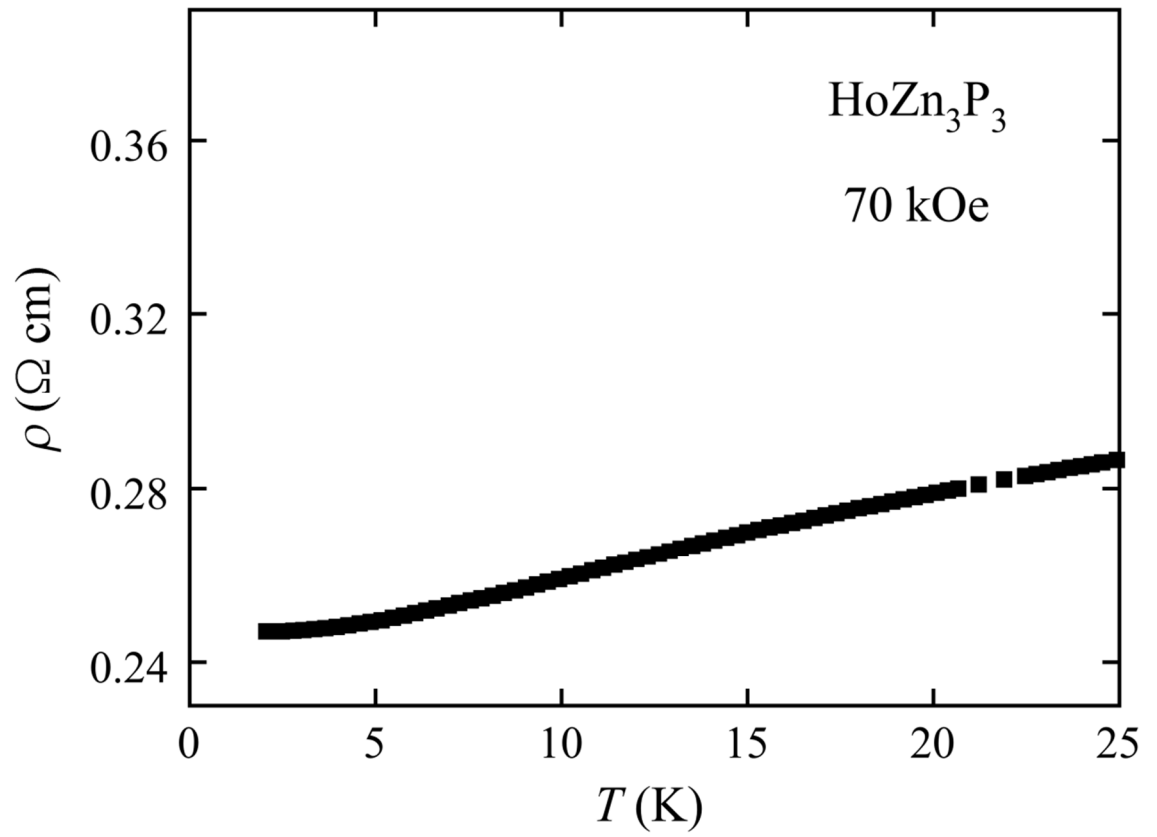
Figure 3.41 Temperature dependence of electrical resistivity of HoZn₃P₃ at 70 kOe below 25 K.
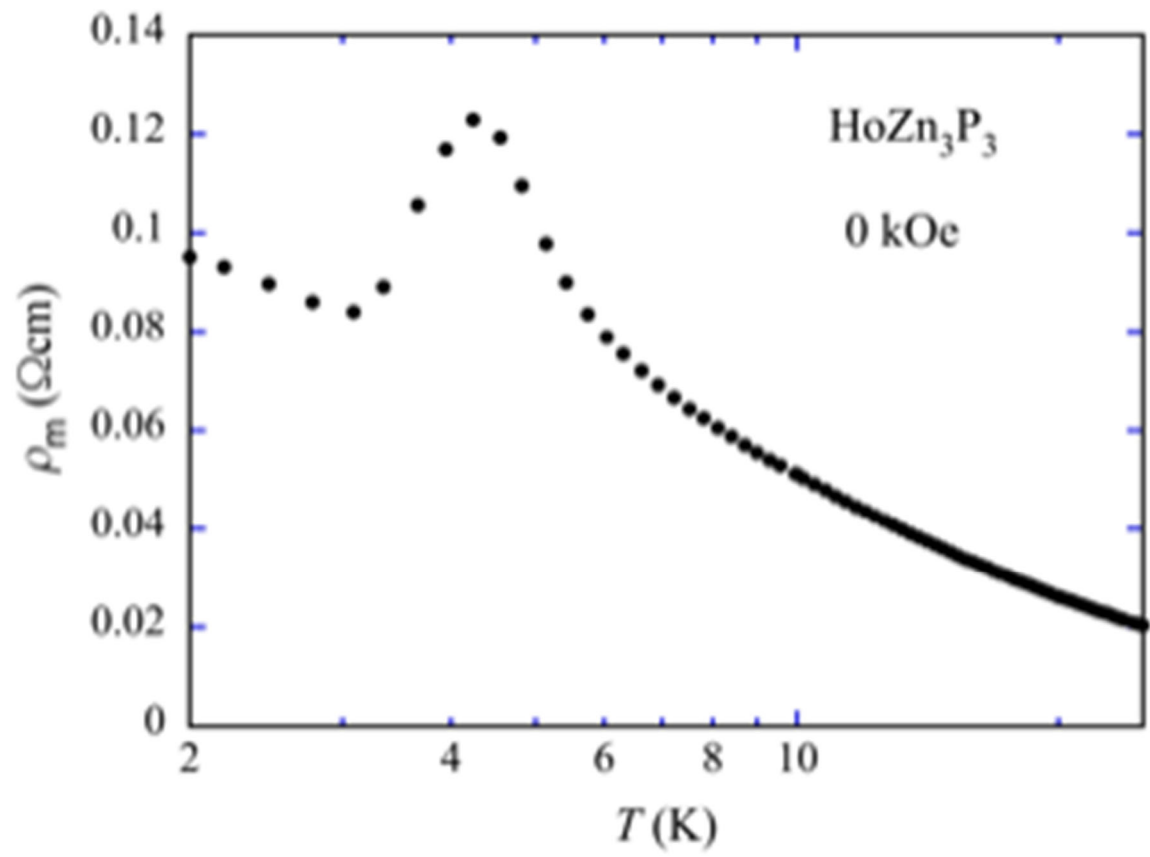
Figure 3.42 Temperature dependence of magnetic resistivity of HoZn₃P₃ at 0 kOe below 25 K.
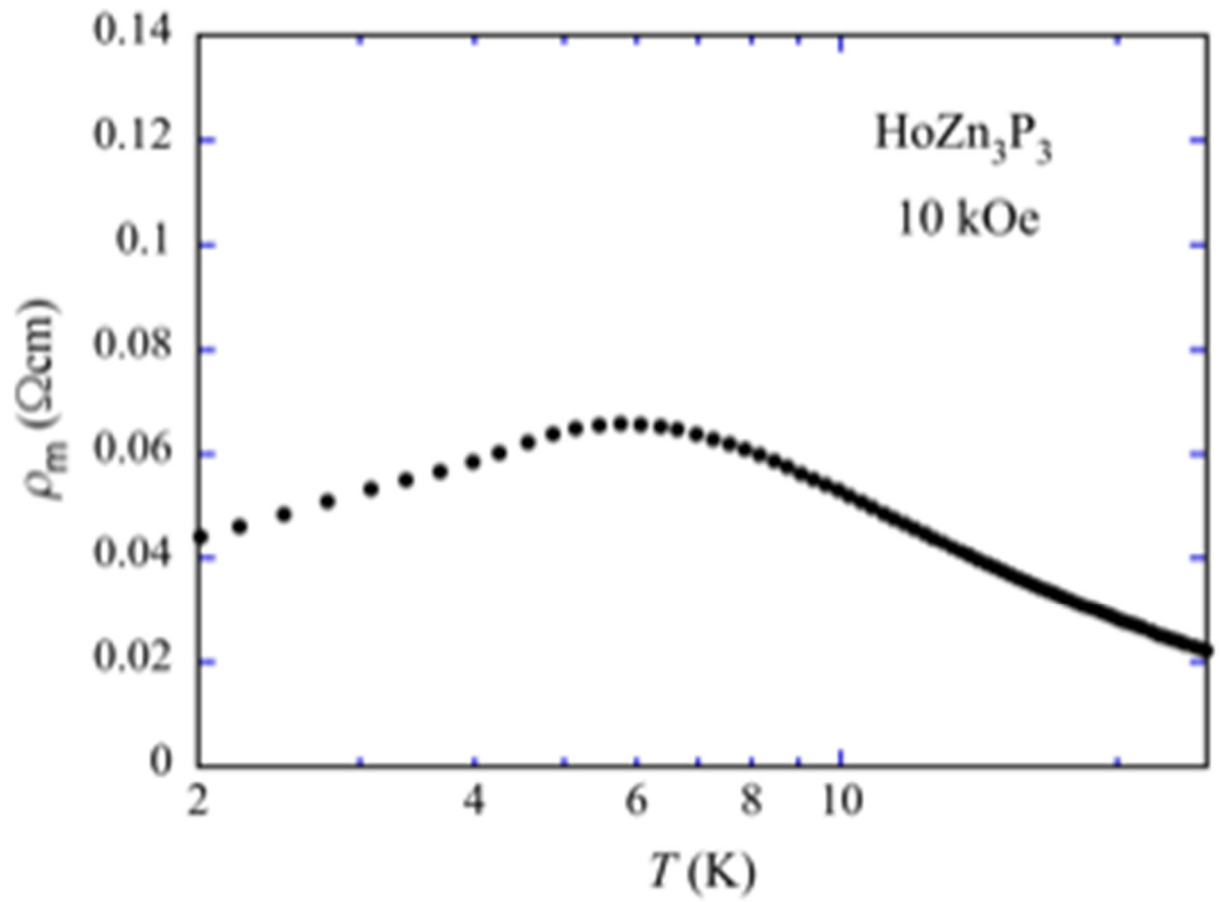
Figure 3.43 Temperature dependence of magnetic resistivity of HoZn₃P₃ at 10 kOe below 25 K.
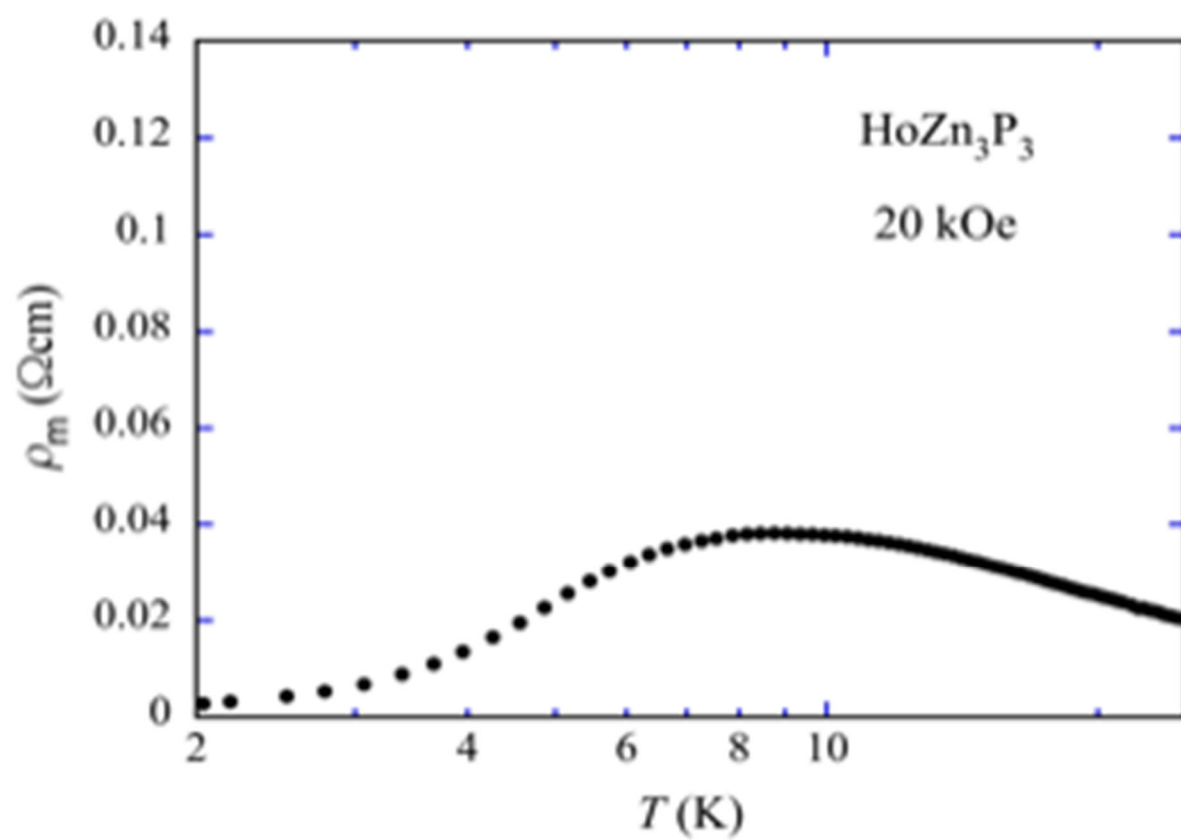
Figure 3.44 Temperature dependence of magnetic resistivity of HoZn₃P₃ at 20 kOe below 25 K.

The magnetic contribution to the resistivity (ρ_m) was calculated by deducing electric and lattice contribution to the resistivity by means of the resistivity at 70 kOe data in low temperature. The ρ_m follows negative logarithmic dependency at low temperature which indicates the possibility of Kondo interaction of localized 4 f electrons with free electrons and other interaction. $HoZn_3P_3$ is the only compound shows Kondo effect so far among rare earth based 1-3-3 RM_3X_3 (R = Rare earth, M = Al, Cd, Zn and X = C, P, As) besides $CeZn_3P_3$ compound which shows photoinduced Kondo effect at high temperature. No structural transition is observed in this compound like other compounds such as $CeCd_3P_3$, $CeCd_3As_3$, and $YbAl_3P_3$.

Figure 3.43 shows volume V of the unit cell and ratio of c/a of RZn_3P_3 compounds [10] [18]. The V decreases as atomic number of R increases due to lanthanide contraction. The ratio c/a reaches minimum at R = Pr or Ce atoms above that increases as atomic number increases. We think unit cell volume and c/a behaviour might be related to deciding electrical nature of the $RZn3P3$. Fig. 3.44 shows magnetic transition temperature T_N, T_M and de-gennes factor G = $(g_J-1)^2$ J (J+1) of RZn_3P_3. From $GdZn_3P_3$, same tendency could follow if RKKY interaction influence compound. A large difference of T_M might be due to other interaction like multipole moment.
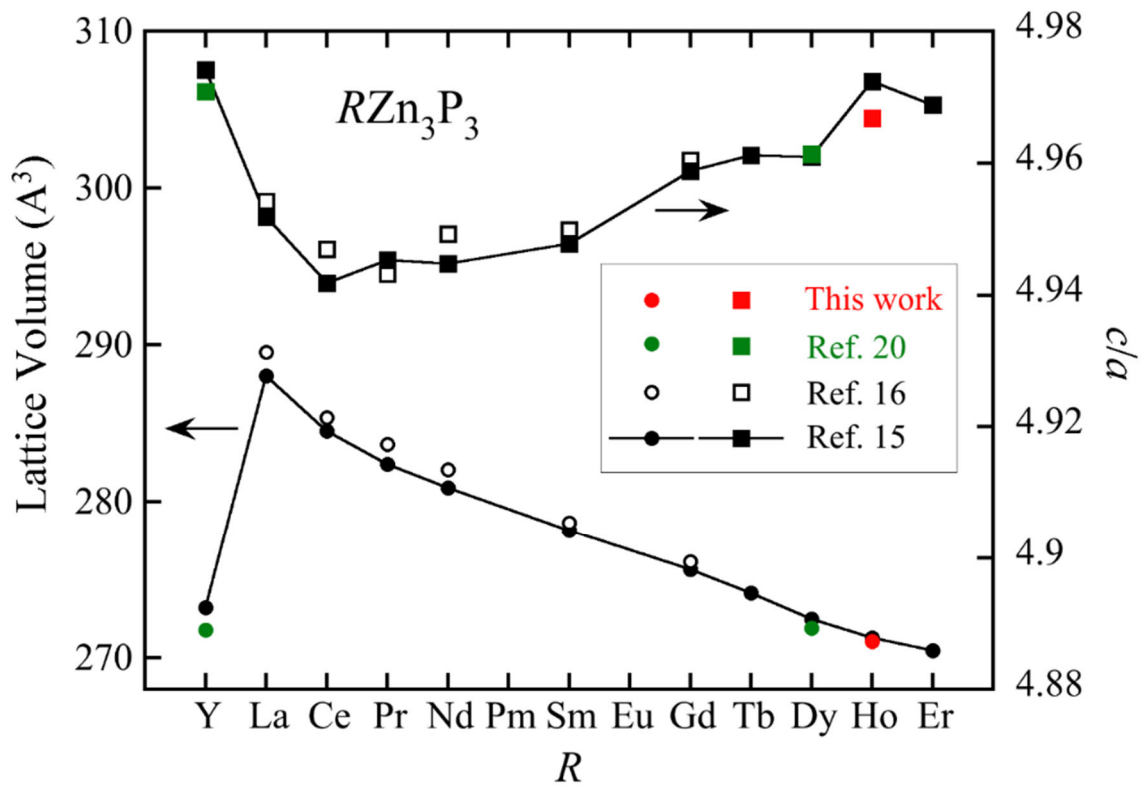
Figure 3.45 Volume and the ratio of *c/a* of *R*Zn₃P₃ compounds.
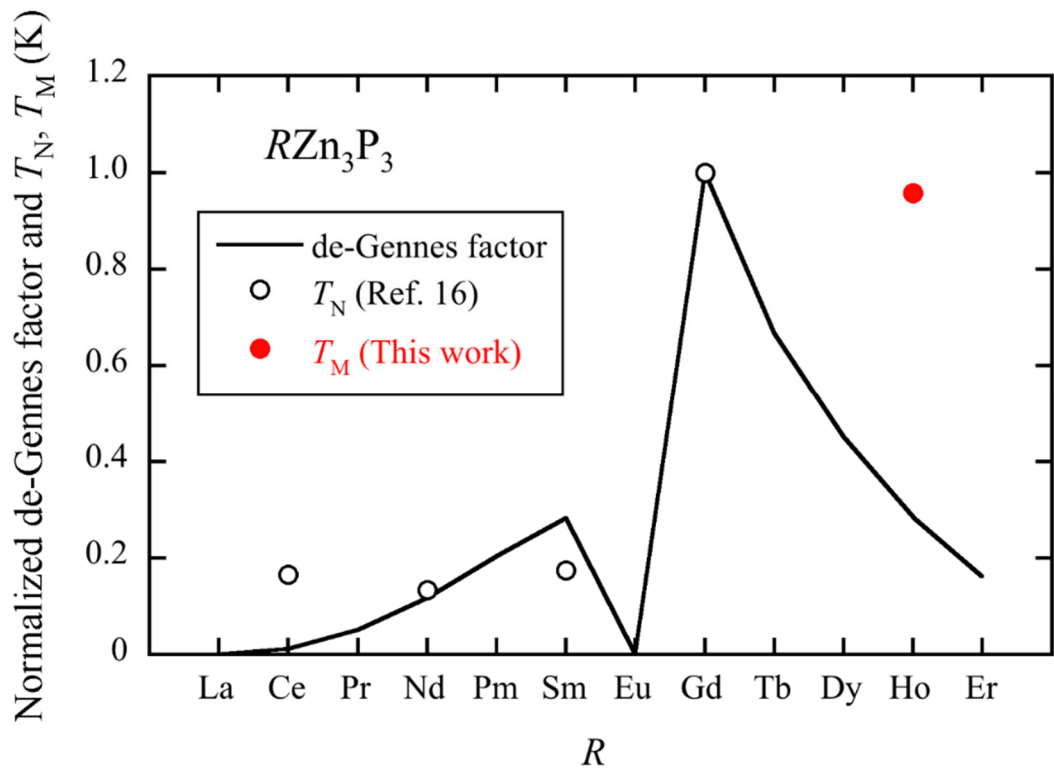
Figure 3.46 Normalized magnetic transition temperature T_N, T_M and de-gennes factor of RZn$_3$P$_3$ by values of GdZn$_3$P$_3$.

CHAPTER – 4

SUMMARY

Conclusion

We have successfully prepared $HoZn_3P_3$ sample under high pressure high temperature method. Magnetic susceptibility, electrical resistivity and specific heat capacity were studied, and the results suggest canted ferromagnetic or ferromultipole ordering at T_M = 4.5 K. Electrical resistivity shows metallic nature at high temperature and Kondo effect at low temperature. Specific heat kind shifts to high temperature with applied field at the rate of 0.06 K/kOe. Electronics specific heat coefficient of 199 mJ/ mol k^2 is observed at 0 kOe and increases to maximum of 660 mJ/mol K^{2}under 60 kOe. A significant amount of entropy is released above T_M. From our results we suggest that RZn$_3$P$_3$ system is novel system to study RKKY interaction, Kondo effect, and geometric frustration. With our limited results we could not confirm the ground state properties of $HoZn_3P_3$ compound. Hence, further measurements are required such as NMR, muon spin spectroscopy and neutron scattering experiments.

References

1) P. W. Anderson, Mater. Res. Bull. **8,** 153 (1973).

2) L. Balents, Nature **464,** 199 (2010).

3) T.-H. Han, J. S. Helton, S. Chu, D. G. Nocera, J. A. Rodriguez-Rivera, C. Broholm and Y. S. Lee, Nature **492,** 406 (2012).

4) J. M. Hopkinson, S. V. Isakov, H.-Y. Kee and Y. B. Kim, Phys. Rev. Lett. **99**, 037201 (2007).

5) Y. Okamoto, M. Nohara, H. Aruga-Katori and H. Takagi, Phys. Rev. Lett. **99**, 137207 (2007).

6) C. Balz, B. Lake, J. Reuther, H. Luetkens, R. Schönemann, T. Herrmannsdörfer, Y. Singh, A. T. M. N. Islam, E. M. Wheeler, J. A. Rodriguez-Rivera, T. Guidi, G. G. Simeoni, C. Baines and H. Ryll, Nature Phys **12,** 942 (2016).

7) Y. Li, G. Chen, W. Tong, L. Pi, J. Liu, Z. Yang, X. Wang, and Q. Zhang, Phys. Rev. Lett. **115**, 167203 (2015).

8) W. Liu, Z. Zhang, J. Ji, Y. Liu, J. Li, X. Wang, H. Lei, G. Chen, and Q. Zhang, Chin. Phys. Lett. **35**, 117501 (2018).

9) M. M. Bordelon, E. Kenney, C. Liu,T. Hogan, L. Posthuma, M. Kavand, Y. Lyu, M. Sherwin, N. P. Butch, C. Brown, M. J. Graf, L. Balents and S. D. Wilson,Nat. Phys. **15,** 1058 (2019).

10) A. T. Nientiedt and W. Jeitschko, J. Solid State Chem.**146**, 478 (1999).

11) Y. Kato, M. Kosaka, H. Nowatari, Y. Saiga, A. Yamada, T. Kobiyama, S. Katano, K. Ohoyama, H. S. Suzuki, N. Aso, and K. Iwasa, J. Phys. Soc. Jpn. **77**, 053701 (2008).

12) K. Hara, S. Matsuda, E. Matsuoka, K. Tanigaki, A. Ochiai, S. Nakamura, T. Nojima and K. Katoh, Phys. Rev. B **85**, 144416 (2012).

13) A. Ochiai, T. Inukai, T. Matsumura, A. Oyamada and K. Katoh, J. Phys. Soc. Jpn. **76**, 123703 (2007).

14) J. Lee, A. Rabus, N. R. Lee-Hone, D. M. Broun and E. Mun, Phys. Rev. B **99**, 245159 (2019).

15) S. R. Dunsiger, J. Lee, J. E. Sonier and E. D. Mun, Phys. Rev. B **102**, 064405 (2020).

16) A. Yamada, N. Hara, K. Matsubayashi, K. Munakata, C. Ganguli, A. Ochiai, T. Matsumoto and Y. Uwatoko, J. Phys.: Conf. Ser. **215**, 012031 (2010).

17) J. Kitagawa, D. Kitajima, K. Shimokawa and H. Takaki, Phys. Rev. B **93**, 035122 (2016).

18) N. Kabeya, T. Sakamoto, K. Hara, Y. Hara, S. Nakamura, K. Katoh and A. Ochiai, J. Phys. Soc. Jpn. **89**, 074707 (2020).

19) C. Sekine and Y. Mori, Jpn. J. Appl. Phys. **56**, 05FA09 (2017).

20) C. Sekine, H. Osanai, K. Ikemori, R. Nakajima, S. Deminami, J. Sirimart and H. Gotou, ES Materials & Manufacturing, **1**, 35 (2018).

21) P. K. Das, N. Kumar, R. Kulkarni and A. Thamizhavel, Phys. Rev. B **83**, 134416 (2011).

22) K. Katoh, S. Nakagawa, G. Terui and A. Ochiai, J. Phys. Soc. Jpn. **78**, 104721 (2009).

23) K. Katoh, E. Honda, T. Matsuo, S. Nakamura, T. Nojima and A. Ochiai, Physica B **429**, 63 (2013).

24) S. Yadam, D. Singh, D. Venkateshwarlu, M. K. Gangrade, S. S. Samatham and V. Ganesan, Bull. Mater. Sci. **39**, 537 (2016).

25) A. D. Hillier, D. T. Adroja, S. R. Giblin, W. Kockelmann, B. D. Rainford and S. K. Malik, Phys. Rev. B **76**, 174439 (2007).

26) M. Jaime, R. Movshovich, G. R. Stewart, W. P. Beyermann, M. G. Berisso, M. F. Hundley, P. C. Canfield and J. L. Sarrao, Nature**405**, 160 (2000).

27) D. Kumar, J. Sankar, J. Narayan, R. K. Singh and A. K. Majumdar, Phys. Rev. B**65**, 094407 (2002).

28) Y. Xu, J. Zhang, G. Cao, C. Jing and S. Cao, Phys. Rev. B**73**, 224410 (2006).